PHYSICAL REVIEW D VOLUME 44, NUMBER 7 1 OCTOBER 1991

Calculations of prompt-photon production in QCD

Edmond L. Berger
High Energy Physics Division, Argonne National Laboratory, Argonne, Illinois 60439

Jianwei Qiu
Institute for Theoretical Physics, State University of New York, Stony Brook, New York 11794-3840

(Received 19 February 1991)

Cross sections for prompt-photon production at collider energies are not strictly inclusive because an isolation requirement is imposed whereby the photon is detected only if accompanied by a restricted amount of hadronic energy. In this paper we provide a consistent treatment of the isolated prompt-photon cross section in QCD perturbation theory. The isolation requirement reduces sensitivity of the cross section to poorly known long-distance fragmentation contributions. However, the normal cancellation of infrared singularities is upset by the isolation cutoffs, rendering the short-distance perturbative calculation highly nontrivial. In our solution we address both the short- and the long-distance issues in detail, showing that well-behaved predictions can be derived for a wide range of isolation parameters. Calculated cross sections are presented at several energies and scale dependence of the cross section is examined.

I. INTRODUCTION

The quantitative reliability of calculations done within the context of perturbative quantum chromodynamics (QCD) is an issue of importance whether one's focus is testing the theory or computing backgrounds in searches for new physics. In the specific case of *inclusive* prompt-photon production at large values of transverse momentum (p_T), the basic theory is particularly simple [1]. For example, in nucleon-nucleon interactions at fixed-target energies, the dominant QCD subprocess in lowest-order perturbation theory is one in which an incident quark interacts with an initial gluon: $qg \to \gamma q$. Correspondingly, provided that calculations can be done well enough, it is generally believed that measurements of $NN \to \gamma X$ would determine the distribution of gluons in a nucleon, $g(x)$. Analogous statements may be made about prompt-photon production at large values of transverse momentum in proton-antiproton interactions at CERN and Fermilab collider energies, $\bar{p}p \to \gamma X$. However, important theoretical issues must be addressed before data at collider energies can be used directly.

In this paper, we examine the uncertainties inherent in perturbative calculations of prompt-photon production. We treat in detail the very important difference between the *inclusive* prompt-photon cross section and the cross section for *isolated* prompt-photon production [2]. At large p_T, a photon can be produced through a pointlike, perturbatively calculable hard-scattering term, as well as through a nonperturbative fragmentation process (generalization of the bremsstrahlung process). Because of the nonperturbative nature of the fragmentation process, perturbative QCD alone cannot predict the size of the prompt-photon cross section. To establish whether definitive constraints on the gluon distribution may be obtained from the data, it is necessary to examine theoretical uncertainties associated with any given order of the perturbative calculation.

We may mention several types of uncertainties. First, there are intrinsic theoretical uncertainties associated with the choices of the renormalization, factorization, and fragmentation scales. Second, there are more prosaic uncertainties related to the imperfect determination of required parton distributions from other processes (notably deep-inelastic lepton scattering), and in particular, to the lack of knowledge of the fragmentation functions which specify the probabilities for quarks and gluons to fragment into photons. To the extent that one's ambition is to determine the gluon distribution and Λ_{QCD} from prompt-photon data, it is important to understand and control these uncertainties. Third, and most important, experiments detect isolated photons at collider energies [3]. This experimental constraint must be imposed on theoretical calculations in order to compare the theory with data. Imposition of the isolation cut threatens to make the theoretical calculation ill defined since the possibility arises that infrared divergences will be introduced [4].

The first class of uncertainty, scale dependence, can in principle be addressed by calculations of the higher-order corrections to the short-distance hard-scattering part of the cross section. In practice, however, it is difficult to calculate the corrections beyond the next-to-leading-order. The next-to-leading order calculation has been done in perturbative QCD for the one-photon inclusive cross section [5–7]. We will use the available result to study and to understand the size of uncertainties associated with the choice of scales. The second class of uncertainty can be addressed only through independent and more precise experimental measurements. At present, we do not have photon fragmentation functions which are as well measured as other parton distributions. Whether the uncertainty associated with the photon fragmentation functions prevents us from extracting reliable information on the gluon distribution from the direct photon data is one of the main issues that we will address in this paper.

At low energy, or at large $x_T = 2p_T/\sqrt{s}$, we find that the inclusive cross section is dominated by processes in which the photons arise directly from short-distance hard scattering. Consequently, the next-to-leading-order QCD calculation, with the inclusion of a model of the fragmentation functions, is expected to and does show reasonable agreement between theory and data for the one-photon inclusive cross section at fixed-target energies [8]. However, at high energy, or at small x_T, the fragmentation process is important and even dominant.

The third issue is that of photon isolation. In this paper we expand on previous work [2] in which we showed that the cross section for prompt-photon production with an *isolation cut* is a perturbatively well-defined quantity. The isolated cross section is much less sensitive to photon fragmentation functions, enabling us to use the high-energy prompt-photon data to determine the small-x behavior of the gluon distribution. In this paper, we present a detailed description of the proper evaluation of such isolated cross sections for prompt-photon production in perturbation theory, and give an all-orders argument to show that the isolated cross section is perturbatively well defined.

Additional uncertainties should be mentioned. These include the role of higher-twist contributions [9] and intrinsic transverse momentum of the incident partons, and nuclear target dependence. Higher-twist and intrinsic-transverse-momentum effects may be of substantial relevance at fixed-target energies where values of p_T are relatively small. Nuclear target effects at fixed-target energies induce broadening of the p_T distribution and, correspondingly, complicate the extraction of $g(x)$. We will not discuss either nuclear effects or high-twist contributions in this paper.

This paper is organized as follows. In Sec. II, we present a general factorized form for the one-photon *inclusive* cross section in Eq. (2.1), and we describe in detail the evaluation of the short-distance hard part $\hat{\sigma}_{ij,c}$. We provide a prescription for handling the singularities associated with the Feynman diagrams when $\hat{\sigma}_{ij,c}$ is evaluated, and we also give a physical picture to $\hat{\sigma}_{ij,c}$ at the parton level. In Sec. III, we explain how to define a cross section with an isolation cut in perturbation theory and how to evaluate it. We argue that such an isolated cross section is perturbatively finite order by order, and that the convergence of this perturbative expansion is no worse than that of the corresponding inclusive cross section. In Sec. IV, we provide calculations of the prompt-photon cross sections at $\sqrt{s} = 630$ GeV, $\sqrt{s} = 1.8$ TeV, and $\sqrt{s} = 400$ GeV, and we present results of our numerical study of the uncertainties associated with the theoretical predictions. Finally, we summarize our conclusions in Sec. V.

II. INCLUSIVE PROMPT-PHOTON PRODUCTION IN QCD

In high-energy hadron-hadron interactions, the observed photons can be produced directly through short-distance hard scattering at the parton level and through the long-distance fragmentation of quarks and gluons, as well as of intermediate photons. Thus, in general, the inclusive cross section for prompt photon production at large transverse momentum has the factorized form

$$E_\gamma \frac{d\sigma^{\text{tot}}}{d^3p_\gamma}(A+B\to\gamma+X) = \sum_{i,j}\int_{x_a}^{1} dx_1 f_{i/A}(x_1,\mu_f)\int_{x_b}^{1} dx_2 f_{j/B}(x_2,\mu_f) \times \sum_{c=\gamma,q,g}\int_{z_{\min}}^{1}\frac{dz}{z^2}\,D_{\gamma/c}(z,\mu_F)\,\hat{\sigma}_{ij,c}(p_c,x_1,x_2,z,\mu,\mu_f,\mu_F)\,, \tag{2.1}$$

where A and B refer to initial hadrons, i and j label the types of incident partons (gluons, quarks, and antiquarks), and c labels a final parton emerging from the short-distance process. The functions f and D are parton distribution and fragmentation functions, respectively. In parton language, these functions are interpreted as probability densities. For example, $f_{i/A}(x_1,\mu_f)dx_1$ is the probability to find a parton of type i in the hadron A with the parton's (light-cone) momentum between x_1 and $x_1 + dx_1$ times its parent hadron's incident momentum. Similarly, $D_{\gamma/c}(z,\mu_F)dz$ is the probability to find a photon in the parton of type c with the photon carrying (light-cone) fraction between z and $z + dz$ of its parent parton's momentum. The integration limits x_a, x_b, and $z_{\min}$ are fixed by kinematics. The parameters μ, μ_f, and μ_F are renormalization, initial-state factorization, and fragmentation scales, respectively. $\hat{\sigma}_{ij,c}$ is a perturbatively calculable short-distance cross section for the subprocess $i + j \to c + X$. Its normalization is specified by the definition (or choice) of f and D.

To evaluate Eq. (2.1), we must compute $\hat{\sigma}_{ij,c}$, have sets of parton distributions f's and photon fragmentation functions D's, and determine the scales μ, μ_f, and μ_F. In principle, $\hat{\sigma}_{ij,c}$ can be calculated perturbatively in QCD perturbation theory. The f's and D's are nonperturbative functions, and they must be measured through a number of different experiments. The scales μ, μ_f, and μ_F are unphysical parameters whose appearance is an artifact of the perturbative calculation to a finite order. Their values cannot be determined from first principles.

The uncertainty due to the choice of these parameters should be considered as a theoretical systematic uncertainty.

A. Calculations of $\hat{\sigma}_{ij,c}$

$\hat{\sigma}_{ij,c}$ is the parton-parton hard scattering cross section for the subprocess $i+j \to c+X$. It may be expressed as a perturbative expansion in the strong coupling strength $\alpha_s(\mu)$:

$$\hat{\sigma}_{ij,c} = A_{ij,c}\,\alpha_s^n(\mu)\,[1 + B_{ij,c}\,\alpha_s(\mu) + \cdots] \; . \qquad (2.2)$$

Up to order $\alpha_s^2(\mu)$ in $\hat{\sigma}_{ij,c}$, the expression for $\alpha_s(\mu)$ in Eq. (2.2) is

$$\alpha_s(\mu) = \frac{4\pi}{\beta_0 \ln \mu^2/\Lambda^2}\left[1 - \frac{\beta_1}{\beta_0}\,\frac{\ln\ln \mu^2/\Lambda^2}{\ln \mu^2/\Lambda^2} + O\left(\frac{1}{\ln^2 \mu^2/\Lambda^2}\right)\right] , \qquad (2.3)$$

where $\beta_1 = (306 - 38N_f)/3$, $\beta_0 = (33 - 2N_f)/3$, and N_f is the number of quark flavors. The renormalization scale μ in Eq. (2.2) is expected to be of the same size as the large momentum invariants in the parton-scattering subprocess, controlled by p_T, the transverse momentum of the observed photon. The effect of the different choices of μ will be discussed below. When the scale μ rises above the thresholds of heavy-quark masses, i.e., $\mu = m_b$ or $\mu = m_t$, we use the same expression for $\alpha_s(\mu)$ but with different values of N_f and Λ. We determine the new Λ by requiring the strong coupling strength α_s to be a continuous function of μ. For example, when μ passes through m_b, we find Λ_5 (the five-flavor value of Λ) from the equation $\alpha_s(\mu = m_b,\ N_f = 5,\ \Lambda_5) = \alpha_s(\mu = m_b,\ N_f = 4,\ \Lambda_4)$ [10].

In Eq. (2.2) the leading- and next-to-leading-order terms A and B are functions of kinematic invariants. The calculation of A is straightforward. It involves calculations of $2 \to 2$ *tree* diagrams. If the photon is produced directly through hard scattering ($c = \gamma$), the expression for A is obtained from the QCD "Compton," $qg \to \gamma q$, and annihilation, $q\bar{q} \to \gamma g$, subprocesses, and the power $n = 1$ in Eq. (2.2). These subprocesses are sketched in Fig. 1. If the photon is produced through parton fragmentation ($c = q$ or g), the expression for A is derived from the tree-level $2 \to 2$ parton-parton scattering diagrams, and the power $n = 2$. Some sample processes are shown in Fig. 2. In all these cases, the A's are *finite* because of the requirement of large p_T. They have neither explicit dependence on the scales μ, μ_f, and μ_F, nor explicit dependence on the scheme used to define the nonperturbative functions, f and D.

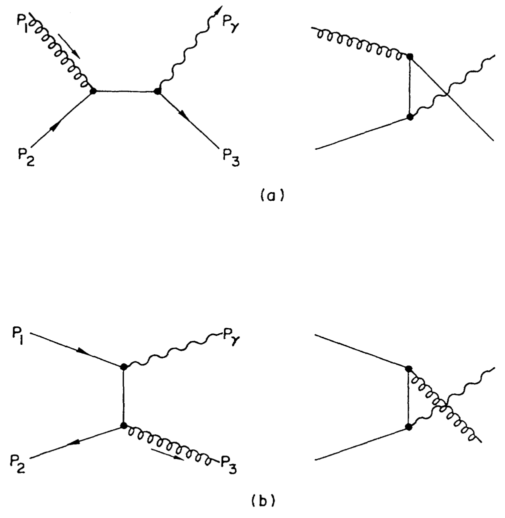

FIG. 1. Diagrams for the subprocesses: (a) gluon-quark to photon-quark (or "Compton"), and (b) quark-antiquark to photon-gluon (or annihilation).

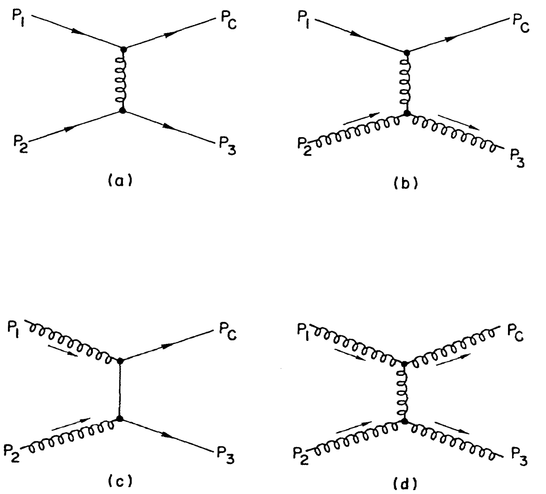

FIG. 2. Some sample diagrams for the leading $2 \to 2$ subprocesses *without* a photon in the short-distance hard part.

The calculation of B is more complicated. The function B depends not only on the scales μ, μ_f, and μ_F, but also on the scheme used to define the f and D. For a calculation valid up to order $\alpha_s^2(\mu)$ for the hard-scattering term $\hat{\sigma}_{ij,c}$, we need to consider the function B only in the case $c = \gamma$. In this case, we must calculate the two parton $\to \gamma +$ one parton one-loop interference diagrams, illustrated in Fig. 3(a), and calculate the tree diagrams for $2 \to \gamma + 2$ subprocesses, such as $qg \to qg\gamma$, $qq \to qq\gamma$, $gg \to q\bar{q}\gamma$, illustrated in Figs. 3(b)–3(d), respectively. These diagrams have ultraviolet and collinear divergences, as well as infrared divergences. The infrared divergence associated with real emission of a soft gluon is canceled exactly by a corresponding divergence in one-loop interference diagrams. This is a result of factorization — the short-distance hard part $\hat{\sigma}$ has no infrared singularity. The renormalization of the ultraviolet divergence in the one-loop interference diagrams introduces the μ dependence of B. When the gluon of momentum p_4, shown in Fig. 3(b), is parallel to the incident

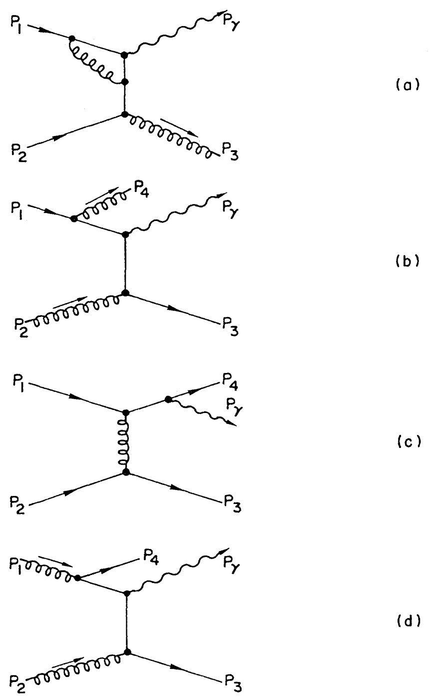

FIG. 3. Some sample diagrams for the next-to-leading-order $\alpha_{\mathrm{EM}}\alpha_s^2$ subprocesses.

quark of momentum p_1, the diagram develops an initial-state collinear singularity. The treatment of this initial-state collinear divergence is standard. The initial-state collinear divergences are absorbed into the parton distributions through the subtraction terms which are needed to avoid double counting. The subtraction procedure introduces the μ_f dependence of B. Different values of μ_f are equivalent to moving finite portions of the product between the hard part and the parton distributions, in addition to moving the collinear poles. Larger μ_f means more is attributed to the parton distributions. Similarly, when the quark of momentum p_4, shown in Fig. 3(c), is parallel to the outgoing photon, the diagram develops a final-state collinear singularity (or bremsstrahlung singularity). If the momentum p_4 is parallel to photon's momentum p_γ, the contribution has already been included in the leading fragmentation contribution, $A_{ij,q}$, via a quark-photon fragmentation function. Therefore, when we calculate the hard part, $B_{ij,\gamma}$ from the diagrams which have final-state collinear singularities [e.g., such as the one shown in Fig. 3(c)], we must introduce a subtraction term, just as is done for the initial-state collinear singularities, in order to avoid double counting. For example, the subtraction term for the diagram shown in Fig. 3(c) is equal to $A_{qq,q}$ convoluted with the leading-order parton level quark-photon fragmentation function. As a result of such subtractions, those final-state collinear singularities of the $2 \rightarrow \gamma + 2$ subprocesses that are associated with a photon becoming parallel with the parton from which it was emitted are absorbed into the photon fragmentation functions $D_{\gamma/q}$. Correspondingly, the function $B_{ij,\gamma}$ becomes dependent on μ_F in addition to μ and μ_f.

When we calculate the hard part $\hat{\sigma}_{ij,c}$ beyond the next-to-leading order in α_s, we have to deal with nonleading corrections $\hat{\sigma}_{ij,c}$ with $c \neq \gamma$. Beyond the order of $2 \rightarrow 2$ tree diagrams, the diagrams contributing to $\hat{\sigma}_{ij,c}$ can have both soft and collinear singularities, just like the diagrams contributing to $\hat{\sigma}_{ij,\gamma}$. The soft singularities are removed when contributions from all virtual and real diagrams are added together. The initial-state collinear singularities are again absorbed into the parton distributions in a standard way. The final-state collinear singularities associated with the parton c, when its momentum is parallel to its parent's momentum, are absorbed into the nonperturbative photon fragmentation functions $D_{\gamma/c}$, with $c = q, g$ as well as $c = \gamma$. For example, to calculate the order of α_s^3 contributions to $\hat{\sigma}_{ij,c}$, we must calculate the functions $B_{ij,c}$ with $c \neq \gamma$. The diagrams shown in Figs. 4(a)–4(d) all contribute to the function $B_{ij,c}$ with $c \neq \gamma$. In this case, the measured photon results from fragmentation of the quark (or gluon) of momentum p_c. In this example, the diagrams shown in Figs. 4(a)–4(d) all have final-state collinear singularities when momentum p_4 is parallel to p_c. Similar to the diagram in Fig. 3(c), when p_4 is parallel to p_c, the diagrams shown in Figs. 4(a) and 4(b) are already included in the leading term, $A_{qq,q}$ convoluted with $D_{\gamma/q}$. This can be seen from the example shown in Fig. 4(f). The splitting from the quark to quark in Fig. 4(a) [or quark to gluon in Fig. 4(b)] is part of the fragmentation function $D_{\gamma/q}$. We can easily find a similar example for the initial-state collinear singularities. For example, when p_4 is parallel to p_1, it is clear that the splitting from the quark to quark in Fig. 3(b) [or gluon to quark in Fig. 3(d)] is just a part of the quark distribution of an incoming hadron. In a fashion very similar to the treatment of the initial-state collinear singularities, when we calculate the hard part $\hat{\sigma}_{ij,c}$ with $c \neq \gamma$ from the diagram shown in Fig. 4(a), we need a subtraction term $A_{qq,q}$ convoluted with the leading-order quark-to-quark splitting (or fragmentation) function. Similarly, for the diagrams shown in Figs. 4(b)–4(d,) subtraction terms are proportional to the corresponding A convoluted with a leading-order parton-to-parton splitting (or fragmentation) function. The diagram shown in Fig. 4(e) also has a final-state collinear singularity when p_4 is parallel to p_c. This diagram is not a leading-order diagram in the electroweak coupling constant α_{EM}. Nevertheless, it shows why the photon-to-photon fragmentation function $D_{\gamma/\gamma}$ is generally needed in Eq. (2.1). The final-state collinear singularity in the diagram shown in Fig. 4(e) is absorbed into the function $D_{\gamma/\gamma}$.

We conclude from the above discussion that the hard-scattering term $\hat{\sigma}_{ij,c}$ in Eq. (2.1) is a perturbatively finite quantity. It can be understood as a parton-level $2 \rightarrow 1$ inclusive cross section with all *collinear* contributions along the directions of momenta p_i, p_j, and p_c subtracted. The collinear contributions are absorbed into the long-distance parton distribution and fragmentation functions. The scales μ_f and μ_F define the sizes of the collinear contributions. A larger scale means more is subtracted. For example, the scale μ_F defines a region

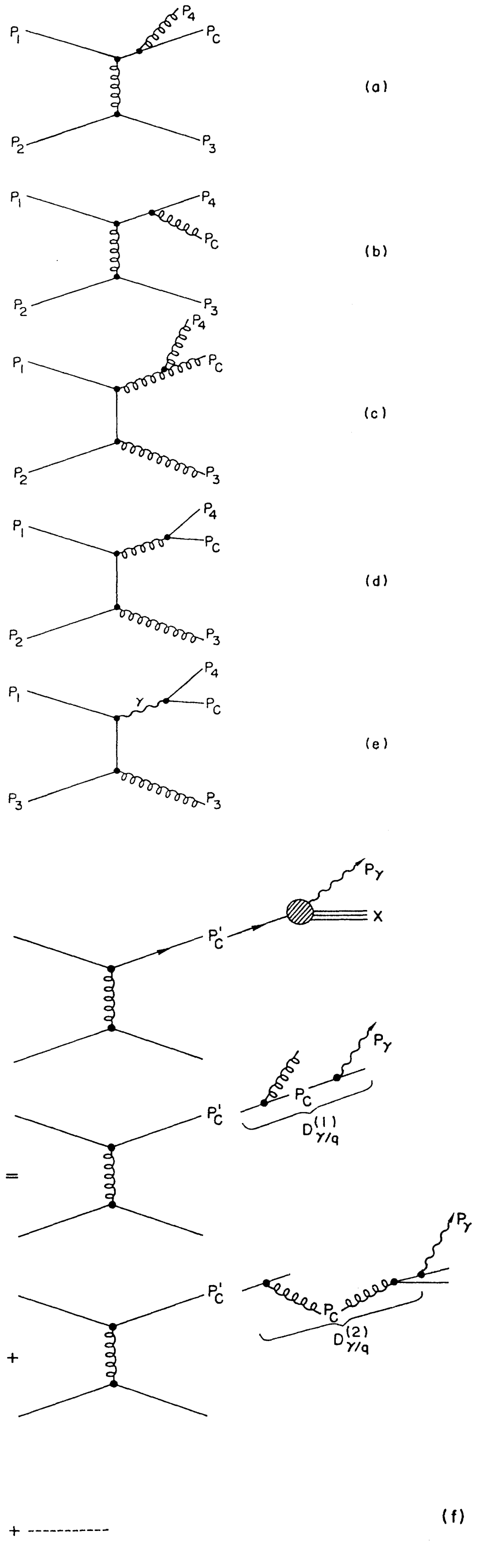

FIG. 4. (a)–(d) Some sample diagrams for the next-to-leading-order α_s^3 subprocesses *without* a photon in the short-distance hard part. (e) A sample high-order diagram in $\alpha_{\rm EM}$. (f) A diagrammatic representation of a process in which the photon is produced through a quark fragmentation function.

around the direction of momentum p_c, such, that at the parton level, $\hat\sigma_{ij,c}$ is like an "isolated" cross section with *no* final-state partons from collinear splitting in that region. Of course, final-state partons can be in the region defined by μ_F *if* the final-state partons are not from splitting of the final-state parton under discussion.

The theoretical calculation of $B_{ij,\gamma}$, the next-to-leading contribution to the hard part $\hat\sigma_{ij,c}$ has been done in perturbative QCD for the one-photon *inclusive* cross section [5, 6]. When a next-to-leading-order expression is used for $\hat\sigma_{ij,c}$ in Eq. (2.1), it is certainly preferable in principle also to use next-to-leading-order evaluations of the parton distributions f and the fragmentation functions D. The extent of knowledge of these nonperturbative functions directly affects the predictive power of Eq. (2.1).

B. Determination of the nonperturbative functions

Many sets are available of parton distributions f determined from fits to data from deep-inelastic lepton scattering of neutrinos, muons, and electrons, sometimes with constraints supplied from massive-lepton pair production and/or prompt-photon production in hadron-hadron interactions. Different emphases placed on the selection of sometimes contradictory deep-inelastic data are reflected in different final parton densities for both quarks and gluons. Fits based on next-to-leading-order QCD have been published recently. These include the parton densities of Diemoz *et al.* [11] (DFLM) which we shall use in this paper, Martin *et al.* [12], and Morfin and Tung [13]. Different sets of parton densities are provided by DFLM corresponding to a range of choices of α_s or $\Lambda_{\rm QCD}$, viz., $\Lambda_{\rm QCD}$ = 160, 260, and 360 MeV. The values of Λ are correlated fairly strongly with the behavior of the x dependence of the gluon density. Thus, the different sets labeled by Λ correspond to different gluon densities. It is of interest to see whether prompt-photon data may discriminate among these sets. The values of Λ quoted above are those appropriate for four flavors.

For the photon fragmentation functions D's, the situation is very different from that of parton distributions. There are not yet any next-to-leading-order photon fragmentation functions. Model photon fragmentation functions are available based on leading-logarithm evolution and vector-meson dominance [14]. In principle, fragmentation functions, just like the parton distributions, should be determined and refined through different experiments. For example, one can try to extract photon fragmentation functions from the cross sections for one-photon inclusive or one-photon plus two-jet data in e^+e^- scattering processes. Although the available simple photon fragmentation functions can roughly fit earlier experimental data [15], because of large experimental uncertainty, we must allow for possibly large alterations to the fragmentation functions, in particular, in the small-z region. As a result, it is perhaps best to state that the available photon fragmentation functions will give us a reliable prediction for hadronic prompt photon production, *iff* the contribution to the cross section from the fragmentation subprocesses is much *smaller* than that from direct short-distance production. Otherwise, it is better to use such direct photon experiments to determine the photon fragmentation functions.

Using the available photon fragmentation functions, we find that at fixed target energies, the fragmentation process contributes less than 10% of the total one-photon inclusive cross sections, whereas at collider energies, it can provide over 50% of the total inclusive cross sections. Therefore, we conclude that Eq. (2.1) will give a reliable prediction for *inclusive* processes only at relatively low energies. However, as we will show later, at collider energies, the photon isolation restriction make theoretical predictions less sensitive to nonperturbative fragmentation functions, restoring predictability of the theory.

C. Choice of scales

The expression for the next-to-leading-order term B in Eq. (2.2) depends on the choice of μ_f and μ_F, on the choice of μ, and on the scheme used to define the parton distribution and fragmentation functions. We consider each of these in turn.

Different choices of μ_f or μ_F are equivalent to moving finite pieces between the nonperturbative functions f and D and the hard-scattering term B in Eq. (2.2). Different choices of the renormalization scale μ modify B by a term having an extra power in α_s.

The dependence of B on the factorization scale μ_f or on the fragmentation scale μ_F is apparent because of the evolution of the parton distributions and the fragmentation functions. For example, the evolution of the type-i parton distribution of hadron h, $f_{i/h}(x,\mu_f)$, with changes in μ_f is expressed through

$$f_{i/A}(x,\mu_f) = f_{i/A}(x,\mu_f^0) + \frac{\alpha_s(\mu_f^0)}{\pi}\ln\left(\frac{\mu_f}{\mu_f^0}\right)\sum_j \int_x^1 \frac{dy}{y} f_{j/A}(y,\mu_f^0)P_{ij}\left(\frac{x}{y}\right) + \cdots . \tag{2.4}$$

In Eq. (2.4), $P_{ij}(z)$ is the appropriate Altarelli-Parisi splitting function relating partons i and j.

The dependence of B on the choice of the renormalization scale μ appearing in $\alpha_s(\mu)$ is apparent from the expression

$$\alpha_s(\mu) = \alpha_s(\mu_0)\left[1 - \frac{33-2N_f}{12\pi}\alpha_s(\mu_0)\ln\left(\frac{\mu^2}{\mu_0^2}\right)\right] + \cdots . \tag{2.5}$$

Finally, B depends on the scheme used to define the parton distributions and photon fragmentation functions. In the case of quark distributions, the standard reference process is deep-inelastic lepton scattering. The quark distributions may be defined such that the structure function $F_2(x,\mu_f)$ is expressed as

$$F_2(x,\mu_f) = x\sum_i e_i^2\left[f_{i/h}(x,\mu_f) + f_{\bar{i}/h}(x,\mu_f)\right], \tag{2.6}$$

with *no* $O(\alpha_s)$ correction, normally called the deep-inelastic scattering (DIS) scheme. In Eq. (2.6), e_i is the charge of the quark of flavor i. A definition different from Eq. (2.6) would result in an order-α_s correction to Eq. (2.6) and to a corresponding change in B in Eq. (2.2). It is important to emphasize that when using next-to-leading parton distributions, one has to make sure that the scheme used in defining the distributions is the same as the scheme used in defining $\hat{\sigma}_{ij,c}$.

If the terms in Eq. (2.2) were computed to all orders in α_s, then the results of Eq. (2.1) would not depend on the choices of scales μ, μ_f, and μ_F. Any change in μ or μ_f or μ_F would alter the relative magnitudes of the different terms in the series expansion in α_s, leaving the sum unaltered. However, for calculations done through a finite order in α_s, there necessarily is dependence on the choices of μ, μ_f, and μ_F.

There are several approaches to the matter of μ, μ_f, and μ_F dependences. We may vary the scales μ, μ_f, and μ_F over a "reasonable" range of values and examine the resulting band of values of the cross section. This band constitutes one estimate of the theoretical systematic uncertainty in our final result. This is the approach we shall adopt. For inclusive prompt-photon production at large p_T, it seems clear to us that the scales μ, μ_f, and μ_F should be about equal to the momentum transfer which occurs in the physical hard-scattering process. Otherwise, one is left to explain the occurrence of disparate scales in the problem. Furthermore, in order to avoid the large logarithms due to mismatch of different scales, we normally choose all scales μ, μ_f, and μ_F in Eq. (2.1) to be of the same size as the large momentum invariant in the parton scattering subprocess, which is p_T. We choose to vary the scales from $p_T/2$ to $2p_T$. There is no requirement that $\mu = \mu_f = \mu_F$, but such a choice simplifies the discussion. It is made in some of our calculations.

Other approaches have been advocated for selecting preferred choices of the scales μ, μ_f, and μ_F. One might choose the scales so that the term B in Eq. (2.2) is very small. This approach, called the fastest apparent convergence [16] (FAC), is predicated on the hope that the unknown yet higher-order terms will also be minimized at the same time. Otherwise, one might determine the scales from imposed supplementary conditions, viz., $\partial\sigma/\partial\mu_f = 0$ and $\partial\sigma/\partial\mu = 0$. This approach is known as the principle of minimal sensitivity [17] (PMS). A similar condition might also be imposed for μ_F. The supplementary conditions are true, of course, if σ is calculated to all orders in α_s. Neither the FAC or the PMS approach is guaranteed to converge, in the sense that the required values of μ, μ_f, and μ_F may not exist in the region $\mu > \mu^0$, $\mu_f > \mu_f^0$, and $\mu_F > \mu_F^0$ where $\alpha_s(\mu)$ and the functions $f_{i/h}(x, \mu_f)$ and $D_{\gamma/c}(z, \mu_F)$ are well specified. Stated differently, the procedures would not be acceptable if unreasonably large values of $\alpha_s(\mu)$ or unreasonably small values of μ_f and μ_F are derived through application of the procedures. As we will demonstrate explicitly in Sec. IV, one has to be careful in applying the PMS procedure.

III. ISOLATED PROMPT-PHOTON PRODUCTION

As explained in the preceding section, the one-photon inclusive cross section is theoretically well defined, but the theoretical prediction depends heavily on our knowledge of the nonperturbative functions, particularly, of the fragmentation functions. In Eq. (2.1), the value of $z_{\rm min}$ is fixed by kinematics, in particular, by x_T. The smaller x_T is, the smaller $z_{\rm min}$ is. Smaller values of $z_{\rm min}$ mean that the cross section is more sensitive to the fragmentation functions. Therefore, at high energy, or at small x_T, the fragmentation process is important and even dominant. It follows that the one-photon *inclusive* process at small x_T is *not* a good place to test the theory unless fragmentation functions are known. On the other hand, at collider energies, experiments detect *isolated* photons [3]. In this section, we present a general description of the proper evaluation of the cross section for prompt-photon production with an isolation cut. We will show that the isolation cut is actually an advantage since it makes the theoretical prediction *less* sensitive to nonperturbative fragmentation functions.

We first introduce the terminology and variables which will be used in defining the cross section with an isolation cut. An isolation cone is defined, as shown in Fig. 5, to be a cone of opening angle δ, and whose axis is the direction of the observed photon. This definition can be converted into the isolation parameter R used in experiments [18]; $R = \sqrt{(\Delta\eta)^2 + (\Delta\phi)^2}$. This expression shows that R is the radius of a circle in pseudorapidity (η) and azimuthal angle (ϕ) space. Hence, when $\eta \simeq y = 0$, $R \approx \delta$. If the total hadronic energy E_h in a photon's isolation cone is less than ϵ times the photon's energy E_γ, the photon is said to be *isolated.* Parameter ϵ is the energy resolution parameter. It is a finite number fixed in experiments to control event acceptance. An isolated cross section is the cross section for isolated prompt-photon events. (We note that our definition of δ, Fig. 5, as the half-angle of the cone differs from that used by Aurenche, Baier, Fontannaz, and Schiff [5] (ABFS).)

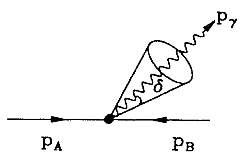

FIG. 5. Diagram illustrating the isolation cone whose axis is the momentum direction of the photon.

For the purpose of the following discussion, it is convenient technically to treat the isolated cross section as the one-photon inclusive cross section *minus* a subtraction term. The subtraction term is the cross section for photons with accompanying hadronic energy greater than ϵE_γ in the isolation cone. Because the one-photon inclusive cross section is perturbatively well defined, to study the behavior of the isolated cross section is to study the subtraction term, which depends only on the events in which photons are accompanied by more than ϵE_γ hadronic energy in the isolation cone. If we use the isolation cone to define a jet, the subtraction term may actually be thought of as a "jet" cross section for jets having a photon and hadronic energy *greater* than ϵE_γ.

The subtraction term is just a part of the one-photon inclusive cross section (or is a "jet" cross section). It should have a factorized form similar to that given in Eq. (2.1). The calculation of the subtraction term should be the same as that for the one-photon inclusive cross section, but with a limited phase space. When the observed photons come from a fragmentation process, we must show how an isolation cut can be imposed on the nonperturbative quantities, the fragmentation functions. We must also address the possible noncancellation of infrared singularities due to the fact that the isolation cut restricts the phase space for integration of the momenta of soft gluons. In addition, because several new scales (the cone size δ and momentum fraction ϵ) are introduced, we should also estimate the effect of possibly large logarithms in high-order corrections caused by the mismatch of different scales.

A. Isolation cut on the fragmentation functions

When a photon is produced through the fragmentation of a quark or a gluon, the event has the character of a photon accompanied by a hadronic jet in the direction of the photon. Because of the nonperturbative nature of fragmentation functions, we do not know theoretically how the hadronic energy is distributed within the fragmentation jet. Therefore, for an arbitrarily defined fragmentation function, when we impose an isolation cone around the photon, we must try to estimate how much hadronic energy from fragmentation will fall into the cone or fall outside of the cone.

Because of the freedom in defining fragmentation functions, we can include the isolation cone as part of the definition of the fragmentation functions, provided the cone size is large enough. If the cone size is too small, the separation of soft and hard contributions will attribute too much of the cross section to hard scattering, rendering the perturbative calculation unreliable. Fragmentation functions, including the isolation restriction, can be measured in principle through different processes in which the same definition is employed. For example, such functions can be measured in isolated photon production in e^+e^- scattering. The fragmentation functions defined through the isolation cone can be related to other definitions by a convolution with perturbatively calculable coefficients (or kernels). The fragmentation functions with different definitions should have the same scale dependence on μ_F because all valid fragmentation functions should have the same long-distance behavior.

As discussed in Sec. II, the fragmentation scale μ_F is a scale that determines how much of the finite contribution of a diagram is included in the nonperturbative fragmentation functions and how much in the hard-scattering part. A larger value of μ_F means more is included in the fragmentation function (or in the fragmentation jet), and the jet size is bigger. Therefore, in calculating the isolated cross section, μ_F should be chosen small enough so that the whole jet is small enough to fall within the isolation cone. Then, the subtraction term for the fragmentation contribution is

$$
\begin{aligned}
&E_\gamma \frac{d\sigma^{\text{sub}}}{d^3p_\gamma}(\text{due to fragmentation}) \\
&\quad = \sum_{i,j} \int dx_1 f_{i/A}(x_1,\mu_f) \int dx_2 f_{j/B}(x_2,\mu_f) \\
&\qquad \times \sum_{c=q,g} \int_{z_{\min}}^{1/(1+\epsilon)} \frac{dz}{z^2}\, \bar{D}_{\gamma/c}(z,\mu_F(\delta))\, \hat{\sigma}_{ij,c}(p_c,x_1,x_2,z,\mu,\mu_f,\mu_F(\delta),\delta,\epsilon)\,. \qquad (3.1)
\end{aligned}
$$

In Eq. (3.1), the upper limit on the z convolution is determined as follows. If p_c is the total momentum of a fragmentation jet, the photon's energy is equal to z times the jet momentum, $E_\gamma = z\,p_c$; and the total hadronic energy within the jet is $E_h = (1-z)\,p_c$. By the definition of the isolated cross section, we allow some hadronic energy, but not more than ϵE_γ, into the isolation cone. This gives the upper limit of the z convolution for the subtraction term, $z < 1/(1+\epsilon)$, because $(1-z)\,p_c > \epsilon E_\gamma = \epsilon\, z\, p_c$. The functions $\bar{D}_{\gamma/c}(z,\mu_F(\delta))$ with $c = q$ and g are the fragmentation functions defined using the isolation cone. Up to order of $\alpha_s^2(\mu)$, the hard-scattering cross section $\hat{\sigma}_{ij,c}(p_c,x_1,x_2,z,\mu,\mu_f,\mu_F(\delta),\delta,\epsilon)$ in Eq. (3.1) is simply equal to the cross section for the tree $2 \to 2$ processes, and it has no dependence on δ or ϵ. However, in general, as we discussed in preceding section, it is equal to an "isolated" $2 \to 1$ parton-level inclusive cross section, and it is a perturbatively well-defined quantity. Its δ and ϵ dependence comes from the effect of the isolation cut on the nonfragmenting final-state partons when these fall within the isolation cone. [The nonfragmenting final-state partons are those which do not arise from final-state parton splitting (or fragmentation) processes; they are not associated with the final-state collinear singularities.]

The import of this discussion is that difficulties associated with the nonperturbative functions are effectively reduced to a definition of fragmentation functions and a choice of the fragmentation scale.

Up to the order of $\alpha_s^2(\mu)$, we can combine Eqs. (2.1) and (3.1) to obtain the prompt-photon cross section due to the isolation cut on the fragmentation process as

$$
\begin{aligned}
&E_\gamma \frac{d\sigma^{\text{iso}}}{d^3p_\gamma}(\text{cut only on fragmentation}) \\
&\quad = \sum_{i,j} \int dx_1 f_{i/A}(x_1,\mu_f) \int dx_2 f_{j/B}(x_2,\mu_f) \\
&\qquad \times \Bigg(\sum_{c=q,g} \int_{1/(1+\epsilon)}^{1} \frac{dz}{z^2}\, D_{\gamma/c}(z,\mu_F)\, \hat{\sigma}_{ij,c}(p_c,x_1,x_2,z,\mu) \\
&\qquad\quad + \sum_{c=q,g} \int_{z_{\min}}^{1/(1+\epsilon)} \frac{dz}{z^2} [D_{\gamma/c}(z,\mu_F) - \bar{D}_{\gamma/c}(z,\mu_F(\delta))] \hat{\sigma}_{ij,c}(p_c,x_1,x_2,z,\mu) \\
&\qquad\quad + \int_{z_{\min}}^{1} \frac{dz}{z^2}\, D_{\gamma/\gamma}(z,\mu_F)\, \hat{\sigma}_{ij,\gamma}(p_\gamma,x_1,x_2,z,\mu,\mu_f,\mu_F) \Bigg)\,. \qquad (3.2)
\end{aligned}
$$

In Eq. (3.2), $\hat{\sigma}_{ij,c}$ is the cross section for the $2 \rightarrow 2$ tree processes with no photon in final state, and $\hat{\sigma}_{ij,\gamma}$ for the $2 \rightarrow 2$ and $2 \rightarrow 3$ processes with one photon in final state. The fragmentation functions $D_{\gamma/c}(z,\mu_F)$ and $\bar{D}_{\gamma/c}(z,\mu_F(\delta))$ can be different in principle because of the freedom in choosing the fragmentation functions for the one-photon inclusive cross section. If we give up this freedom, we choose instead the function $\bar{D}_{\gamma/c}(z,\mu_F(\delta))$ for the inclusive cross section. Then the second term in Eq. (3.2) vanishes, the hard part in the last term becomes dependent on $\mu_F(\delta)$, and the function $D_{\gamma/c}(z,\mu_F)$ in the first term in Eq. (3.2) is replaced by $\bar{D}_{\gamma/c}(z,\mu_F(\delta))$. The interesting point is that with such a choice of the fragmentation functions, the isolated cross section given in Eq. (3.2) depends on the nonperturbative fragmentation functions $\bar{D}_{\gamma/c}(z,\mu_F(\delta))$ only in a very small region of z near $z = 1$. Because the fragmentation functions $\bar{D}_{\gamma/c}(z,\mu_F(\delta))$ with $c \neq \gamma$ should be either finite or vanish as a power of $(1-z)$ as $z \rightarrow 1$, Eq. (3.2) shows that, when ϵ is small, the isolated cross section is dominated by the subprocesses in which the photon is directly produced by short-distance hard scattering. We conclude that if ϵ is small enough, the isolated cross section is much *less* sensitive to nonperturbative fragmentation functions than the fully inclusive cross section.

In a $2 \rightarrow n$ process with $n \geq 3$, it is possible for a final-state quark or gluon with energy larger than ϵE_γ to get into the photon's isolation cone. To define a general isolated cross section, we must subtract such contributions from the cross section given in Eq. (3.2). As we discussed before, the fragmentation functions include all final-state collinear singularities as well as all collinear contributions in a region around the direction of momentum p_c. This region is specified by the scale μ_F. We need, therefore, to subtract nonfragmenting contributions within the isolation cone only from the hard part $\hat{\sigma}_{ij,c}$. The discussion of this issue is given in the next subsection.

We now estimate the fragmentation scale $\mu_F(\delta)$ such that the nonperturbative fragmentation jet can be roughly included in an isolation cone of opening angle δ. The relationship between μ_F and the size of the fragmentation jet cannot be expressed in terms of a simple equation because it depends on the choice of the factorization scheme. It can be estimated best in terms of a transverse-momentum cutoff scheme. When the transverse momentum between the photon and its accompanying partonic fragments is larger than μ_F, we attribute the contribution to hard scattering. Otherwise, we include the contribution in the fragmentation jet. For example, if the photon comes from a quark through bremsstrahlung radiation, we can estimate the relation between μ_F and the cone size δ as $\mu_F(\delta) \approx \delta\, p_q = \delta\, E_\gamma (1-z)/z$, with $z_{\rm min} < z < 1/(1+\epsilon)$, where p_q is the momentum of a quark accompanying the photon. It follows that $\mu_F(\delta)$ is of order δE_γ. Note that when z is near its upper limit, $\mu_F(\delta)$ could be as small as $\epsilon\delta E_\gamma$. This occurs at the edge of phase space where the fragmentation function is very small. More typical values of z, where the fragmentation function is large, are close to $z_{\rm min}$ where $\mu_F(\delta) = \delta E_\gamma (1-z_{\rm min})/z_{\rm min} > \delta E_\gamma$. In general, once we choose a scheme, we can only *approximately* estimate the relation between the value of μ_F and the size of the isolation cone δ. The uncertainty is the theoretical systematic uncertainty due to the choice of the scheme.

Once $\mu_F(\delta)$ is chosen in the fragmentation functions, the short-distance hard-scattering cross section will develop a $\ln(\delta)$ dependence owing to the introduction of a second scale, $\delta\, E_\gamma$, into the problem. If δ is too small, the large $\ln(\delta)$ dependence may cancel a power of α_s and make the perturbative expansion converge slowly. Consequently, the isolated cross section would not be well estimated by the perturbative calculation. The isolation cone used in experiments [3] is small but fortunately not so small that $\ln(\delta)$ is large.

In general, to avoid a situation in which $\mu_F(\delta)$ would become too small in the short-distance hard-scattering part, we can fix μ_F to be of order of p_T for the inclusive contribution, and retain the second term in Eq. (3.2) for the isolated cross section. Although the second term in Eq. (3.2) depends on the nonperturbative fragmentation function $\bar{D}$ through $\bar{D}(z,\mu_F) - \bar{D}(z,\mu_F(\delta))$, the size of this term is still small because $\mu_F(\delta)$ is of order $\mu_F \sim p_T$, except when z is near its upper limit $1/(1+\epsilon)$, in which case the fragmentation function is near zero.

B. Contribution of soft gluons

Hadronic energy may enter the isolation cone not only from the fragmentation process but also from the nonfragmenting final-state quarks and/or gluons produced in the short-distance hard scattering. In any $2 \rightarrow \gamma + n$ partonic subprocess, with $n \geq 1$, it is possible for $n-1$ of the n final-state partons to fall into the isolation cone. The other final-state parton must have large p_T to balance the photon's transverse momentum. The subtraction term should include the part of the total cross section for which the nonfragmenting quarks and/or gluons within the cone carry total energy larger than ϵE_γ.

Again, up to order of $\alpha_s^2(\mu)$, we must consider only the $2 \rightarrow 3$ process with one photon in the final state. In this case, only one of the two final-state partons (quark or gluon) can fall into the isolation cone of the photon. The phase space for the parton of momentum k in the cone is

$$\frac{d^3k}{(2\pi)^3 2\omega} \Rightarrow \frac{1}{(2\pi)^3} \int_\delta d\Omega \int_{\epsilon E_\gamma}^{\omega_{\rm max}} \frac{\omega d\omega}{2}\,, \tag{3.3}$$

where ω is the parton's energy, and $\omega_{\rm max}$ is fixed by kinematics. In principle, the subtraction term is perturbatively *finite* for fixed values of δ and ϵ. The issue is whether the perturbative expansion converges fast enough, so that it is unnecessary to compute higher-order corrections to get a reasonable estimate.

When $\delta \rightarrow 0$ and $\epsilon \rightarrow \omega_{\rm max}/E_\gamma$, the subtraction term vanishes. As we will show explicitly below, when δ is finite and $\epsilon \rightarrow 0$, there is an infrared divergence. This is exactly what we expect because a *completely* isolated cross section, with absolutely no hadronic energy in the isolation cone, is not a perturbatively well-defined quantity for a massless particle. However, the value of ϵ is fixed experimentally to be finite. The question of interest is for what values ϵ becomes so small that the subtraction

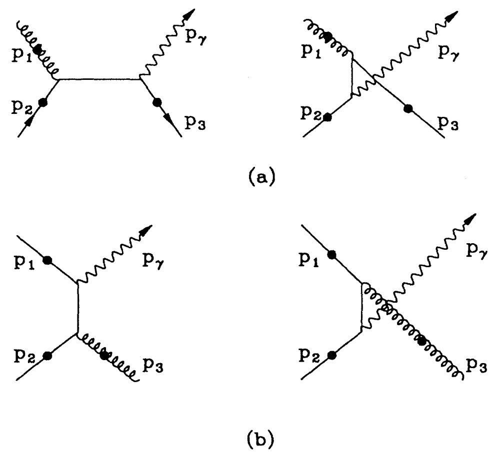

FIG. 6. Diagrams for the subprocesses (a) gluon-quark to photon-quark and (b) quark-antiquark to photon-gluon. The large dots on the external lines are locations at which a soft gluon emission may be attached.

term is too big (or is infrared divergent).

To investigate this question, we study the behavior of the subtraction term when ϵ is *small.* When ϵ is small, only soft gluons, not quarks, will produce a possible infrared divergence. As discussed below, the matrix element associated with soft-gluon emission is proportional to $1/\omega^2$. When combined with the $\omega d\omega$ phase-space factor, Eq. (3.3), the soft gluons yield a $\ln\epsilon$ divergence. On the other hand, the matrix element for soft-quark emission is proportional to $1/\omega$, resulting in no divergence for quarks. We will use the soft-gluon approximation [19] to examine the leading behavior as ϵ goes to zero. The dominant contribution of $2 \to 3$ processes as $\epsilon \to 0$ is given by diagrams shown in Fig. 6. In these diagrams, the dots are the places where a soft-gluon may be attached. Notice that we show only dots on the external lines because the soft-gluon attachments on the internal lines will not give the leading behavior as gluon's momentum goes to zero. The leading contribution of diagrams in Fig. 6 can be written as

$$\hat{\sigma}_{2\to 3} \approx g^2 \int_\delta \frac{d\Omega}{(2\pi)^3} \int_{\epsilon E_\gamma}^{\omega_{\max}} \frac{\omega d\omega}{2}\left(\frac{1}{\omega^2}\right)\left|\varepsilon^*_\alpha\left(C_1\frac{p_1^\alpha}{p_1\cdot\hat{k}} + C_2\frac{p_2^\alpha}{p_2\cdot\hat{k}} - C_3\frac{p_3^\alpha}{p_3\cdot\hat{k}}\right)\right|^2 \hat{\sigma}_{2\to 2}\ , \tag{3.4}$$

where C_i with $i = 1$, 2, and 3 are color factors associated with the vertex where the soft gluon is attached, ε^*_α is the polarization vector for the soft gluon, and $\hat{k}^\mu = k^\mu/\omega$. In Eq. (3.4), $\hat{\sigma}_{2\to 2}$ is the hard-scattering cross section for the normal $2 \to 2$ process with one photon in the final state, given by the diagrams shown in Fig. 1, but with color factor generally connected with the C_i's. Actually, because the color factor for diagrams in Fig. 1(a) [or in Fig. 1(b)] is the same, we can completely factorize $\hat{\sigma}_{2\to 2}$ including the color factor from $\hat{\sigma}_{2\to 3}$, such that

$$\hat{\sigma}_{2\to 3}(p_\gamma, x_1, x_2, \delta, \epsilon) \approx \Gamma(p_\gamma, x_1, x_2, \delta, \epsilon)\, \hat{\sigma}_{2\to 2}(p_\gamma, x_1, x_2)\ , \tag{3.5}$$

where $\hat{\sigma}_{2\to 2}(p_\gamma, x_1, x_2)$ is the standard leading contribution from a $2 \to 2$ process with one photon in the final state. When the isolation cone δ is small, the function Γ is given by

$$\begin{aligned}\Gamma\ &(p_\gamma, x_1, x_2, \delta, \epsilon)\\ &\approx g^2 \int_\delta \frac{d\Omega}{(2\pi)^3} \int_{\epsilon E_\gamma}^{\omega_{\max}} \frac{\omega\, d\omega}{2}\left(\frac{1}{\omega^2}\right) C(p_\gamma, x_1, x_2)\\ &= \left(\frac{\alpha_s}{\pi}\right)\ \sin^2\left(\frac{\delta}{2}\right)\ \ln\left(\frac{1}{\epsilon}\right) C(p_\gamma, x_1, x_2) + O(\epsilon^0)\ .\end{aligned} \tag{3.6}$$

In deriving Eq. (3.6), we assumed that δ is small. We used the fact that the angle $\theta_{p_i\gamma}$ is large, and we approximate $\theta_{p_i\hat{k}} \approx \theta_{p_i\gamma}$, so that $p_i \cdot \hat{k} \approx \omega_i(1 - \cos(\theta_{i\gamma}))$ does not depend on $d\Omega$. As a result, the quantity C in Eq. (3.6) is approximately independent of parameters δ and ϵ, but it depends on kinematical variables x_1, x_2, and p_γ. For example, for the diagrams in Fig. 6(a), the expression for C is

$$\begin{aligned}C_a = &\left(\frac{1}{N(N^2-1)}\sum_{jl}^{N}\sum_{C}^{N^2-1}|t^C_{lj}|^2\right)^{-1}\\ &\times\frac{1}{N(N^2-1)}\sum_{i,j,k,l}^{N}\sum_{A,B,C}^{N^2-1}\left|\varepsilon^*_\alpha(B)\left(f^{ABC}\delta_{kl}\delta_{ji}\frac{p_1^\alpha}{p_1\cdot\hat{k}} + t^B_{ji}\,\delta^{AC}\delta_{kl}\frac{p_2^\alpha}{p_2\cdot\hat{k}} - t^B_{kl}\,\delta^{AC}\delta_{ji}\frac{p_3^\alpha}{p_3\cdot\hat{k}}\right)t^C_{lj}\right|^2 .\end{aligned} \tag{3.7}$$

The subscript a stands for the diagrams in Fig. 6(a), and the first factor, in the large parentheses, is the color factor for the corresponding $2 \to 2$ tree process. In Eq. (3.7), f^{ABC} is the structure constant of the color group, and t^B_{ji} is the color matrix in the fundamental representation, normalized so that $\mathrm{Tr}(t^A t^B) = \delta^{AB}/2$. One may deduce from Eq. (3.7) that the C's for diagrams in Fig. 6 are *positive*, and are of order 1. We do not need the detailed expression of C here because we are interested only in its sign and magnitude for the following discussion.

Equations (3.5) and (3.6) show that the subtraction term due to soft gluons is infrared divergent if we keep δ fixed and let ϵ go to zero. However, because of the energy resolution of the detector, ϵ can be small but never equal to zero. Consequently, the subtraction term in the definition of the isolated cross section is always perturbatively finite. It could be very large for a tiny ϵ. For isolated cross sections measured in today's experiments, the factor $\Gamma(p_\gamma, x_1, x_2, \delta, \epsilon)$ in Eq. (3.5) for the subtraction term is actually much *smaller* than *unity* because ϵ is not very small [for example, $\epsilon = 0.15$ for the Collider Detector at Fermilab (CDF) experiment], and because the factor $(\alpha_s/\pi)\sin^2(\delta/2)$ is *very* small. Therefore, soft gluons will not destroy the convergence of the perturbative calculation of the isolated cross sections. The fact that the subtraction term for the short-distance hard part $\hat{\sigma}_{ij,\gamma}$ is small explains why the program distributed by Aurenche *et al.* [5] can roughly fit collider data, even though the program is in error in not taking into account the effect of the isolation cut on the short-distance hard part $\hat{\sigma}_{ij,\gamma}$.

To conclude our theoretical discussion of the definition of the isolated cross section, we present the general form for the isolated prompt-photon cross section

$$E_\gamma \frac{d\sigma^{\rm iso}}{d^3p_\gamma}(p_T, y, \delta, \epsilon) = \sum_{i,j} \int dx_1 f_{i/A}(x_1, \mu_f) \int dx_2 f_{j/B}(x_2, \mu_f) \times \sum_{c=\gamma,q,g} \int_{1/(1+\epsilon)}^{1} \frac{dz}{z^2}\, \bar{D}_{\gamma/c}(z, \mu_F(\delta))\, \hat{\sigma}^{\rm iso}_{ij,c}(p_c, x_1, x_2, z, \mu, \mu_f, \mu_F(\delta), \delta, \epsilon)\ . \tag{3.8}$$

Equation (3.8) is a direct extension of Eq. (3.2). It is obtained after the isolation cut is included on the nonfragmenting final-state partons. When the photon is from the hard part, the parton-photon fragmentation function is proportional to $\delta(1-z)$. We ignore the nonleading terms in $\alpha_{\rm EM}$. The partonic hard cross section $\hat{\sigma}^{\rm iso}_{ij,c}$ is provided by the $i + j \to c + X$ subprocess after subtraction of those contributions, for which hadronic energy in the isolation cone (caused by the nonfragmenting final-state partons) is larger than ϵE_γ. The cross section $\hat{\sigma}^{\rm iso}_{ij,c}$ is perturbatively finite. Because of the limits on the z convolution, Eq. (3.8) shows that the isolated cross section for prompt-photon production is much *less* sensitive to the nonperturbative fragmentation functions.

Up to order $\alpha_s^2(\mu)$, the short-distance hard part $\hat{\sigma}_{ij,c}$ in Eq. (3.8) is very simple. When $c \neq \gamma$, $\hat{\sigma}_{ij,c}$ is equal to the partonic cross section for $2 \to 2$ tree-level processes with no photon in the final state. When $c = \gamma$, $\hat{\sigma}_{ij,\gamma}$ has two parts. One is the regular next-to-leading-order (order-α_s^2) term in the inclusive cross section. It depends on the isolation cut only through the fragmentation scale $\mu_F(\delta)$. The other is given by the standard leading-order term minus a subtraction term. That is,

$$\begin{aligned}\hat{\sigma}^{\rm iso}_{ij,\gamma}&(p_\gamma, x_1, x_2, z, \mu, \mu_f, \mu_F(\delta), \delta, \epsilon)\\ &= \hat{\sigma}^{\rm NLO}_{ij,\gamma}(p_\gamma, x_1, x_2, z, \mu, \mu_f, \mu_F(\delta))\\ &\quad + [\,\hat{\sigma}^{\rm LO}_{ij,\gamma}(p_\gamma, x_1, x_2, z, \mu)\\ &\qquad - \hat{\sigma}^{\rm sub}_{ij,\gamma}(p_\gamma, x_1, x_2, z, \mu, \delta, \epsilon)]\ .\end{aligned} \tag{3.9}$$

When ϵ is small, the subtraction term above is proportional to the standard leading-order term, as shown in Eq. (3.5), and the second term in Eq. (3.9) is approximately given by

$$\begin{aligned}\hat{\sigma}^{\rm LO}_{ij,\gamma}&(p_\gamma, x_1, x_2, z, \mu) - \hat{\sigma}^{\rm sub}_{ij,\gamma}(p_\gamma, x_1, x_2, z, \mu, \delta, \epsilon)\\ &\approx [1 - \Gamma(p_\gamma, x_1, x_2, \delta, \epsilon)]\, \hat{\sigma}^{\rm LO}_{ij,\gamma}(p_\gamma, x_1, x_2, z, \mu)\ ,\end{aligned} \tag{3.10}$$

where $\Gamma(p_\gamma, x_1, x_2, \delta, \epsilon)$ is given in Eq. (3.6).

Experimentally, in order to have uniform efficiency to cut off the hadronic background, it may be better to use a *fixed* cut on the hadronic energy, $E_h = {\rm const} \sim 1$ GeV. The parameter ϵ in such a case may be much smaller than the value used in today's experimental analysis. If ϵ is tiny, there is a risk that multiple soft-gluon contributions could destroy the perturbative expansion of the isolated cross section. In this case, the QCD resummation technique for real soft gluons can improve the calculation through exponentiation of the subtraction term [20]:

$$\begin{aligned}1 - \Gamma(p_\gamma, x_1, x_2, \delta, \epsilon) &\Rightarrow e^{-\Gamma(p_\gamma, x_1, x_2, \delta, \epsilon)}\\ &= \epsilon^{(\alpha_s/\pi)\sin^2(\delta/2) C(p_\gamma, x_1, x_2)}\ .\end{aligned} \tag{3.11}$$

Even if ϵ is tiny, Eq. (3.11) shows that the soft-gluon contribution is infrared insensitive after resummation because $C > 0$.

To examine how small ϵ can be before resummation appears to be necessary, we take a specific case of a fixed cut $E_h = 2$ GeV and $E_\gamma = 100$ GeV. In this case $\epsilon = 0.02$, which is much smaller than the value $\epsilon = 0.15$ typical of present experiments. Calculating Γ from Eq. (3.6), we obtain $\Gamma \simeq (\alpha_s/\pi)\, C \sin^2(\delta/2) \ln 50$. Using $R = 0.7$ ($\delta \simeq 40°$) and $\alpha_s(100) \simeq 0.13$, we find $\Gamma \simeq 0.02C$. Equation (3.4) shows that C is a dimensionless quantity of order unity. Thus, even for values of ϵ as small as $\epsilon \simeq 0.02$, $\Gamma \ll 1$ and exponentiation should not be required.

So far we have considered effects associated with production of photons through the long-distance fragmentation process and the contribution of soft gluons. We did not consider the case in which one or more final-state partons, which are not in the photon's isolation cone at the parton level, can fragment into hadrons some of which enter the isolation cone. Such effects should be small if the photon is produced near 90° in the center-of-mass frame, but they might not be small if the photon's rapidity (y) is too large. Thus, we anticipate that theoretical systematic uncertainties may be larger at large rapidity.

Before closing this subsection, we remark that the isolation cut is not implemented properly in the program of ABFS [5]. These authors do not subtract contributions from nonfragmenting final-state partons (quark or gluon) having energy larger than ϵE_γ which enter photon's isolation cone. As a result in the program of ABFS, there is no $\ln(\epsilon)$ divergence when ϵ goes to zero.

C. Dependence on isolation parameters

We have described above how the isolated cross section for prompt-photon production depends on the isolation parameters, the cone size δ (or R) and the energy resolution parameter ϵ. The dependence on ϵ should not be dramatic for a reasonable range of values of ϵ, because the subtraction term is very small in comparison with the leading term [Γ in Eq. (3.10) is much less than 1]. We now show numerically the dependence of the isolated cross section on the isolation parameters.

Two programs are available to calculate an isolated cross section for prompt-photon production [5, 7]. As mentioned above, the isolation cut is not imposed correctly in the ABFS program. Approximations are also found in the program of Baer *et al.* For example, the fragmentation scale μ_F used in the $2 \rightarrow 3$ part of Baer *et al.* is *not* chosen to be $\mu_F(\delta)$, appropriate to the cone size. Thus, the second term on the right-hand side of Eq. (3.2) does not vanish. However, this term is omitted altogether from the program of Baer *et al.* If μ_F is not far from $\mu_F(\delta)$, we will consider ignoring the term an approximation. The isolation constraint is implemented perhaps more properly in the program of Baer *et al.* However, because a Monte Carlo technique is used to do the integrals, considerable time is required to obtain good numerical precision. We use the program of Baer *et al.* to test the numerical dependence on the isolation parameters.

In Fig. 7, we present calculations of the isolated cross section for prompt-photon production at $\sqrt{s} = 1.8$ TeV with different values of ϵ. The isolation cone is fixed by $R = 0.7$, which is the value used by the CDF Collaboration. Since the cross section is nearly independent of rapidity in the central region of rapidity, we fix $y \leq 0.75$. As expected, the isolated cross section is insensitive to the value of ϵ. From Eq. (3.11), we see that smaller ϵ means that the subtraction term is larger. The cross sections shown in Fig. 7 decrease slowly as ϵ gets smaller, as they should.

In Fig. 8, we present similar calculations with different values of isolation cone R, but with a fixed value of ϵ. The points with $R = 0$ are the one-photon inclusive cross sections. When R is large enough, $R \geq 0.4$, the isolated cross section is not very sensitive to the actual value of R.

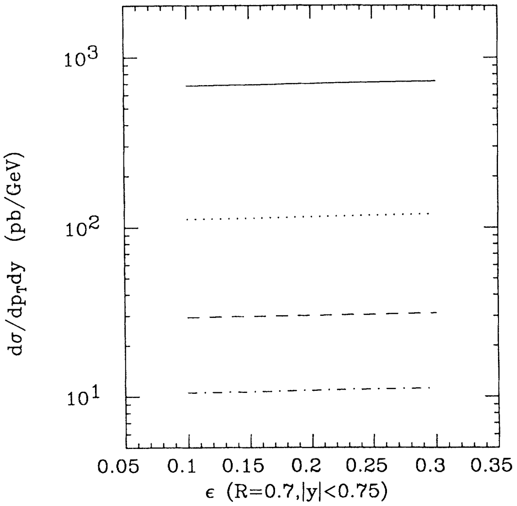

FIG. 7. The cross section for $p\bar{p} \rightarrow \gamma X$ as a function of the energy resolution ϵ at $\sqrt{s} = 1.8$ TeV and at $p_T = 17.5$ GeV (solid), 27.5 GeV (dotted), 37.5 GeV (dashed), and 47.5 GeV (dot-dashed), respectively.

IV. NUMERICAL STUDY

The cross section for production of photons at large transverse momentum in hadron-hadron collisions may be used to test the predictions of perturbative QCD and to constrain the gluon distribution. In this section we present theoretical predictions and discuss their uncertainties.

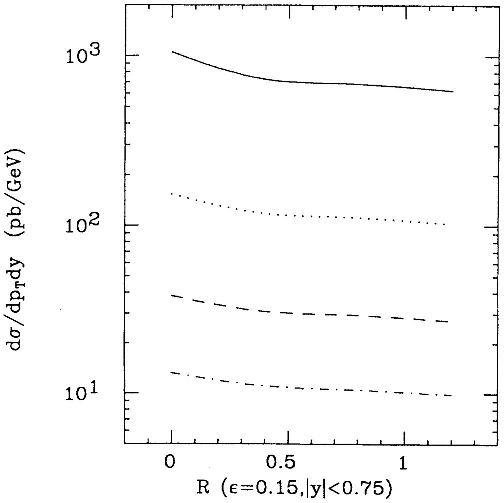

FIG. 8. Dependence of the prompt-photon cross section on the size of the isolation cone R. The notation is the same as that in Fig. 7.

A. Constraints on the gluon distribution

It has been argued that hadronic prompt-photon production is a good probe of the gluon distribution in a hadron. The question of interest is how well hadronic prompt-photon experiments can constrain the gluon distribution. In lowest order in perturbation theory, prompt photons are produced by the QCD "Compton," $qg \to \gamma q$, and annihilation, $\bar{q}q \to \gamma g$, subprocesses. In nucleon-nucleon interactions, the Compton subprocess is essentially always dominant. In proton-antiproton interactions at collider energies, the Compton process is also dominant as long as $x_T = 2p_T/\sqrt{s}$ is not too great. In Fig. 9, we show our *lowest-order* calculations of $E\,d\sigma/d^3p$ for $\bar{p}p \to \gamma X$ at $\sqrt{s} = 630$ GeV and $\sqrt{s} = 1.8$ TeV. Here we use the DFLM set-2 parton distributions, and we set $\mu = \mu_f = p_T$. No fragmentation processes are included at this order. Since the lowest-order hard-scattering cross sections are used in this case, we also use the lowest-order expression for α_s instead of the two-loop expression of Eq. (2.3). Calculations done to next-to-leading order and with a spectrum of values of μ's are discussed below. In Fig. 9 we note that the Compton subprocess is dominant at $\sqrt{s} = 630$ GeV for $p_T \lesssim 45$ GeV. At $\sqrt{s} = 1.8$ GeV, it dominates for $p_T \lesssim 100$ GeV.

The dominance of the Compton subprocess in nucleon-nucleon interactions at fixed-target energies and in $\bar{p}p$ interactions, especially at Fermilab Tevatron energies, suggests that prompt-photon production should be very valuable for extracting the gluon distribution function. At rapidity $y = 0$, the typical value of x of the gluon density is $x = 2p_T/\sqrt{s}$. Greater and lesser values are explored as the rapidity of the prompt γ increases. These values of x are not readily accessible in other processes which provide information on the gluon density.

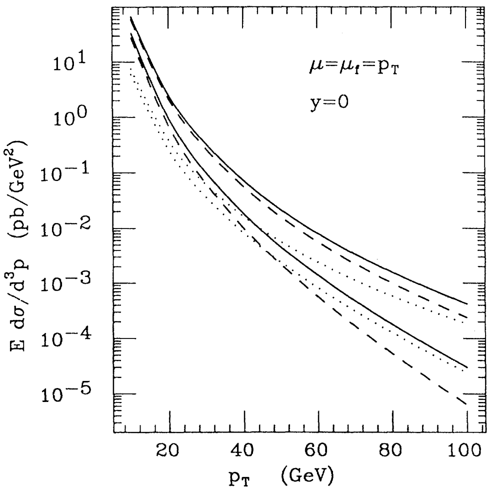

FIG. 9. The cross section $Ed\sigma/d^3p$ for $\bar{p}p \to \gamma X$ as a function of p_T at rapidity $y = 0$ at $\sqrt{s} = 1.8$ TeV (upper set of lines) and at $\sqrt{s} = 630$ GeV (lower set). The solid lines show the total rates in *lowest order*, whereas the dashed and dotted lines show the partial contributions from the lowest-order $qg \to \gamma q$ and $q\bar{q} \to \gamma g$ subprocesses, respectively. The DFLM set-2 parton densities were used with $\mu = \mu_f = p_T$.

To establish whether definitive constraints on the gluon density may be obtained from the data, it is necessary first to examine theoretical uncertainties associated with next-to-leading-order calculations and the variations of the scales, the μ's, as well as the dependence on the nonperturbative fragmentation functions. Useful information on the gluon distribution can be obtained only if these uncertainties are smaller than differences associated with changes in the gluon distribution.

In the rest of this subsection, we will discuss the constraints on the shape of the gluon distribution from the p_T and y dependences of the cross sections, $E\,d\sigma/d^3p$. We use the DFLM parton distributions and the available program by Aurenche *et al.* [5], which includes the next-to-leading-order calculation for the *inclusive* $E\,d\sigma/d^3p$. The photon fragmentation functions [14] used by ABFS are obtained by employing just the leading-logarithmic solutions of the evolution equations. Such solutions are part of the complete solutions of the equations and are actually independent of the boundary condition needed to solve the inhomogeneous evolution equations. Because the leading-logarithmic solutions are proportional to $\alpha_{\rm EM}$, which is very small, the scale at which we can neglect the nonleading terms that depend on the boundary condition must be very large [14]. Consequently, these fragmentation functions are at best an approximation or a model of fragmentation functions. In principle, the photon fragmentation functions should be obtained by solving the evolution equations with input functions at a scale of $\mu_F^0 \gg \Lambda_{\rm QCD}$. The input functions should be obtained by fitting independent experimental data. We should require the scale μ_F^0 to be much larger than $\Lambda_{\rm QCD}$ because the validity of the leading-logarithmic evolution equations is in question when the scale is about the same as $\Lambda_{\rm QCD}$. We set aside these concerns for the moment since our present aim is to investigate how much can be learned from prompt-photon experiments rather than to provide absolute theoretical predictions for cross sections. We use the ABFS program to test the sensitivity of the *inclusive* $E\,d\sigma/d^3p$ to gluon distributions. We defer the discussion of the *isolated* $E\,d\sigma/d^3p$ to the next subsection.

Results of our numerical calculations are shown in Fig. 10 for $E\,d\sigma/d^3p$ at $y = 0$, and in Fig. 11 for $E\,d\sigma/d^3p$ as a function of y. The energies of $\sqrt{s} = 630$ GeV and 1.8 TeV correspond to measurements at CERN and Fermilab, respectively; the curve for $\sqrt{s} = 400$ GeV may be of interest for studies at the Brookhaven Relativistic Heavy-Ion Collider (RHIC). For the calculations in Figs. 10(a), 10(c), 10(d), and 11, we used the DFLM set-2 densities, set $\mu = \mu_f$, and varied μ_f over the range $\frac{1}{2}p_T < \mu_f < 2p_T$. In the program of ABFS, μ_F is set equal to $\sqrt{\hat{s}}$, where $\sqrt{\hat{s}}$ is the center-of-mass energy of the incident parton-parton hard scattering [5]. We observe that changes of μ_f over the indicated range result in about 10% differences in predicted cross sections at $y = 0$ and $p_T = 10$ GeV and about 15% differences at $y = 0$ and $p_T = 80$ GeV. In Table I we present results in numerical form for different choices of parton distributions and different choices of scale. An examination of this table shows that changes in $E\,d\sigma/d^3p$ resulting from variations of μ_f are comparable to and sometimes greater than those associated with changes in the DFLM gluon distribution (i.e., Λ_4).

For purposes of comparison, in Fig. 10(b) we present a calculation based on the program of Baer *et al.*, Ref. [7]. In this program, the leading-order parton densities of Duke and Owens are used, and $\mu_F = p_T$. We will return to a discussion of the comparison of theory and data in Sec. V.

In Figs. 12 and 13 we present our calculations of

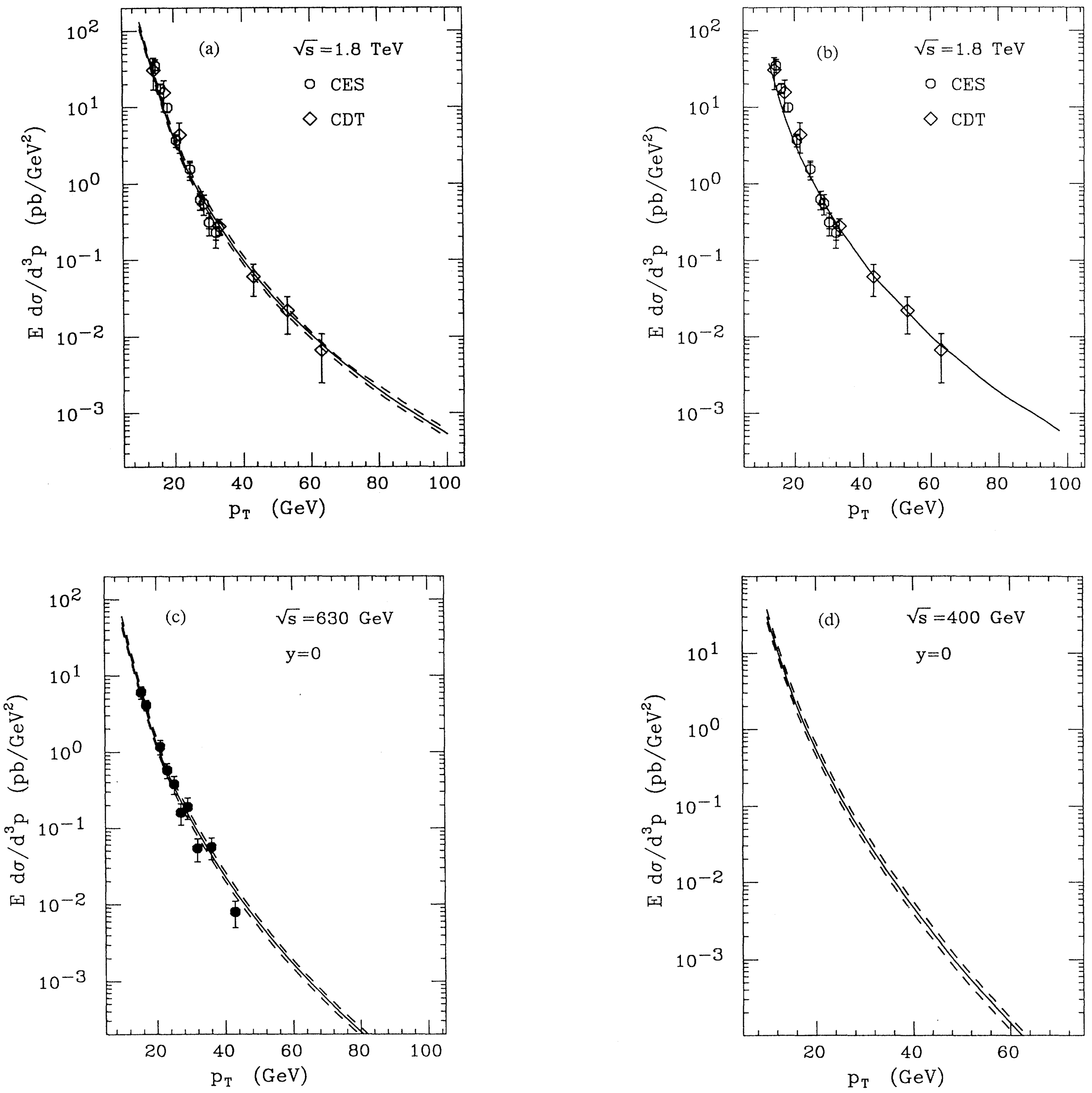

FIG. 10. The cross section $E\,d\sigma/d^3p$ calculated through next-to-leading order at $y = 0$ as a function of p_T at (a), (b) $\sqrt{s} = 1.8$ TeV, (c) $\sqrt{s} = 630$ GeV, and (d) $\sqrt{s} = 400$ GeV. In (a), (b), and (c) we show results for $\bar{p}p \rightarrow \gamma X$; in (d) we show $pp \rightarrow \gamma X$. In (a), (c), and (d) the program of ABFS was used, and in (b) the program of Ref. [7] was used. The solid line shows the prediction for the choice $\mu = \mu_f = p_T$. The upper dashed curve in (a), (c), and (d) corresponds to the choice $\mu = \mu_f = \frac{1}{2}p_T$, whereas the lower dashed curve corresponds to the choice $\mu = \mu_f = 2p_T$. The data in (c) are from the UA2 Collaboration, and those in (a) and (b) are from the CDF Collaboration [3]. In (a) and (b), the data points represented by octagonal symbols were deduced from electromagnetic showers from the electromagnetic strip chambers (CES). Those represented by diamonds were deduced from conversion electrons in drift tubes (CDT). The data in (a), (b), and (c) include a photon isolation cut but the theoretical curves do not.

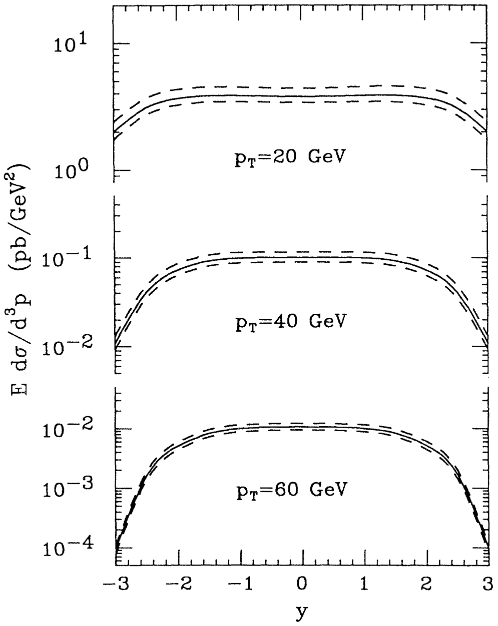

FIG. 11. The cross section $Ed\sigma/d^3p$ for $\bar{p}p \to \gamma X$ calculated through next-to-leading order as a function of y and for selected values of p_T at $\sqrt{s} = 1.8$ TeV. The DFLM set-2 parton densities were used. The solid lines show the prediction for the choice $\mu = \mu_f = p_T$. The upper dashed curves correspond to the choice $\mu = \mu_f = \frac{1}{2}p_T$, whereas the lower dashed curves correspond to the choice $\mu = \mu_f = 2p_T$.

$E\,d\sigma/d^3p$ done instead with the parton distributions of Aurenche, Baier, Fontannaz, Owens, and Werlen [8] (ABFOW). The results are in remarkably close agreement with those shown in Figs. 10 and 11, again suggestive that variations associated with changes in μ_f are greater than those resulting from differences in the gluon distribution.

In the DFLM sets, and in the ABFOW set of parton distributions, the small-x dependence of gluon momentum distribution at its reference value of μ_f^0 is parametrized in nonsingular fashion as $x \to 0$, e.g., $xg(x,\mu_f^0) \to$ const as $x \to 0$. Thus, the relative similarity of final results for $E\,d\sigma/d^3p$ may reflect the similarity of the input gluon distributions. To investigate this question, we considered an alternative form for $xg(x,\mu_f^0)$ having singular low-x behavior, $xg(x,\mu_f^0) \to x^{-1/2}$. Specifically, we use the same quark and antiquark distributions as in the ABFOW set, but we introduce a new gluon distribution:

$$g(x,\mu_f^0) = N\, g_{\text{ABFOW}}(x,\mu_f^0), \quad x > x_0\,,$$
$$g(x,\mu_f^0) = N\left(\frac{x_0}{x}\right)^{1/2} g_{\text{ABFOW}}(x,\mu_f^0), \quad x \le x_0. \tag{4.1}$$

The normalization constant N is fixed by the momentum integral requirement $\int xg(x,\mu_f^0)dx = \int xg_{\text{ABFOW}}(x,\mu_f^0)dx$. We select $x_0 = 0.1$ so that only the small-x behavior of $g(x,\mu_f^0)$ is affected. Our modification leaves the *shape* of the gluon density unaltered at large x, but the magnitude of the density is changed to satisfy momentum conservation. Larger values of x_0 result in smaller magnitudes of the density at large x, where it is constrained to some extent by fixed-target data. The singular behavior of the distribution at small x ($x < x_0$) allows us to examine sensitivity in the low-x region where collider data contribute. The expression in Eq. (4.1) must be evolved to the desired values of μ_f, and we have done so using the evolution program of Morfin and Tung [13].

In Figs. 14 and 15 we show the results we obtained for $E\,d\sigma/d^3p$ based on the singular gluon distribution. Comparing Figs. 13 and 15 we observe clear differences in the y dependences at low p_T, but there is not much difference in the p_T dependences in Figs. 12 and 14. Naively, one would expect that the cross sections shown in Figs. 14 and 15 would be much larger than those shown in Figs. 12 and 13 because the gluon distribution is larger and the Compton process dominates. The key here is momentum conservation. In the case of the singular gluon distribution, gluons are moved from the large-x region to the small-x region. For a given combination of kinetic variables, there is a threshold such that only gluons of momentum fraction larger than $x_{\min}$ contribute to the cross section. If $x_{\min} \gtrsim x_0$, the cross section obtained from the singular gluon distribution will be *smaller* than that obtained otherwise. If $x_{\min}$ is smaller than x_0, but not too much smaller, cross sections will not be sensitive to the choice of the singular distribution. However, if $x_{\min}$ is much smaller than x_0, the cross section will be very sensitive to the singular gluon distribution because of the behavior of the parton-level cross section near the threshold. In our calculation, small p_T corresponds to small $x_{\min}$. The typical value of x_T at $\sqrt{s} = 1.8$ TeV is about 0.01–0.1 for p_T ranging from 10 to 100 GeV. Therefore, one will not see much effect of the singular gluon density for p_T larger than 50 GeV or so. However, the small-p_T region is the region in which an effect may be observed. The y dependence at small p_T directly reflects the shape of the parton densities.

One important way to enhance sensitivity to the x dependence of $g(x)$ is to study the doubly differential distribution $d\sigma/dy_\gamma dy_{\text{jet}} dp_T$. Here y_{jet} is the rapidity of the dominant hadronic jet recoiling against the prompt photon.

B. Effect of isolation cut at different energies

As discussed in the two previous sections, the photon fragmentation function is the key for determining whether prompt-photon data can yield useful information on the gluon distribution. In principle, we cannot provide definitive constraints on the gluon distribution without knowing precisely the photon fragmentation functions. To get practically useful constraints on the gluon distribution from prompt-photon data, it is important to study how sensitively the cross section depends on the nonperturbative photon fragmentation functions.

The presence of the fragmentation functions in the factorized form for the prompt-photon cross section is necessary because these functions absorb all final-state collinear singularities associated with the parton-level Feynman diagrams. The fragmentation functions contribute to the cross sections through the z convolution with the limits from $z_{\min}$ to 1. The smaller $z_{\min}$ is, the more sensitively the cross section depends on the fragmentation functions. The value of $z_{\min}$ is fixed by kinematics, and it is strongly correlated with $x_T = 2p_T/\sqrt{s}$. Larger x_T means larger $z_{\min}$. It is clear then that at low energy, the cross section is less sensitive to the fragmentation functions, while at high energy it depends more on the fragmentation functions. In Fig. 16, we present the ratios of cross sections at different energies $\sqrt{s}$, $E\,d\sigma^{\text{dir}}/d^3p$ divided by $E\,d\sigma^{\text{tot}}/d^3p$, where σ^{dir} is the cross section for photons directly produced from the hard part [i.e., $c = \gamma$ in Eq. (2.1)], while σ^{tot} is the one-photon inclusive cross section. To obtain Fig. 16, we used the program of ABFS, with no isolation cut, and with the approximate leading-logarithmic fragmentation functions. Figure 16 shows that, at low energy, the inclusive cross section is not very sensitive to possible uncertainties in the fragmentation functions. But, at collider energies, the inclusive cross section is very sensitive to the contributions from fragmentation processes, and, consequently, to the fragmentation functions. The one-photon *inclusive* cross section at collider energies is not very useful for measuring gluon distribution unless we know the photon fragmentation functions well.

As discussed in Sec. III, the photon isolation cut reduces the dependence on fragmentation functions. This is because the limits of the z convolution for the isolated cross section are not from $z_{\min}$ to 1, but from $1/(1+\epsilon)$ to 1. The lower limit for the isolated cross section does not depend on any kinematical variable. It is a fixed

TABLE I. Differential cross section $E\,d\sigma/d^3p$ for $\bar{p}p \to \gamma X$ at $\sqrt{s} = 1.8$ TeV for various values of p_T and y. In column 3, the "central value" is obtained for the choice $\mu = \mu_f = p_T$ and the DFLM set-2 parton densities ($\Lambda_4 = 260$ MeV). Columns 4 and 5 show the variation of the result when the parameter $\mu = \mu_f$ is changed from its central value. For columns 6 and 7, $\mu = \mu_f = p_T$ but Λ_4 is changed from its central value.

			μ		Λ_4	
p_T (GeV)	y	$E\,d\sigma/d^3p$	$\frac{1}{2}p_T$	$2p_T$	160 MeV	360 MeV
10.00	0.00	0.1159E+03	0.1309E+03	0.1046E+03	0.9480E+02	0.1334E+03
10.00	1.00	0.1190E+03	0.1357E+03	0.1068E+03	0.9550E+02	0.1397E+03
10.00	2.00	0.1203E+03	0.1370E+03	0.1081E+03	0.9150E+02	0.1496E+03
10.00	3.00	0.1005E+03	0.1135E+03	0.9085E+02	0.7150E+02	0.1337E+03
20.00	0.00	0.3804E+01	0.4434E+01	0.3411E+01	0.3396E+01	0.4028E+01
20.00	1.00	0.3875E+01	0.4553E+01	0.3456E+01	0.3377E+01	0.4208E+01
20.00	2.00	0.3685E+01	0.4376E+01	0.3252E+01	0.3073E+01	0.4191E+01
20.00	3.00	0.2043E+01	0.2444E+01	0.1774E+01	0.1663E+01	0.2391E+01
30.00	0.00	0.4677E+00	0.5376E+00	0.4140E+00	0.4341E+00	0.4787E+00
30.00	1.00	0.4705E+00	0.5447E+00	0.4147E+00	0.4269E+00	0.4931E+00
30.00	2.00	0.4018E+00	0.4745E+00	0.3499E+00	0.3533E+00	0.4355E+00
30.00	3.00	0.1264E+00	0.1539E+00	0.1081E+00	0.1122E+00	0.1365E+00
40.00	0.00	0.1001E+00	0.1148E+00	0.8865E−01	0.9499E−01	0.1008E+00
40.00	1.00	0.9902E−01	0.1144E+00	0.8734E−01	0.9227E−01	0.1016E+00
40.00	2.00	0.7363E−01	0.8703E−01	0.6393E−01	0.6738E−01	0.7708E−01
40.00	3.00	0.1161E−01	0.1425E−01	0.9800E−02	0.1104E−01	0.1176E−01
50.00	0.00	0.2942E−01	0.3363E−01	0.2605E−01	0.2830E−01	0.2935E−01
50.00	1.00	0.2847E−01	0.3279E−01	0.2510E−01	0.2705E−01	0.2878E−01
50.00	2.00	0.1799E−01	0.2121E−01	0.1556E−01	0.1702E−01	0.1831E−01
50.00	3.00	0.1197E−02	0.1461E−02	0.9875E−03	0.1214E−02	0.1141E−02
60.00	0.00	0.1059E−01	0.1204E−01	0.9379E−02	0.1028E−01	0.1051E−01
60.00	1.00	0.9986E−02	0.1145E−01	0.8793E−02	0.9632E−02	0.9978E−02
60.00	2.00	0.5243E−02	0.6151E−02	0.4520E−02	0.5107E−02	0.5206E−02
60.00	3.00	0.1104E−03	0.1325E−03	0.8973E−04	0.1204E−03	0.9842E−04
70.00	0.00	0.4395E−02	0.4973E−02	0.3896E−02	0.4296E−02	0.4349E−02
70.00	1.00	0.4018E−02	0.4590E−02	0.3537E−02	0.3925E−02	0.3979E−02
70.00	2.00	0.1717E−02	0.2008E−02	0.1477E−02	0.1717E−02	0.1666E−02
70.00	3.00	0.6537E−05	0.7861E−05	0.5168E−05	0.7833E−05	0.5314E−05

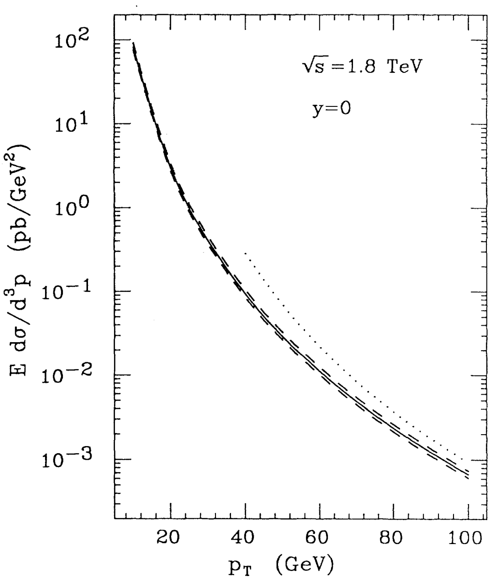

FIG. 12. The cross section $E\,d\sigma/d^3p$ for $\bar{p}p \rightarrow \gamma X$ calculated through next-to-leading order at $y = 0$ as a function of p_T at $\sqrt{s} = 1.8$ TeV. The ABFOW parton densities were used. The solid line shows the prediction for the choice $\mu = \mu_f = p_T$. The upper dashed curve corresponds to the choice $\mu = \mu_f = \frac{1}{2}p_T$, whereas the lower dashed curve corresponds to the choice $\mu = \mu_f = 2p_T$. The dotted line was obtained after application of the PMS scheme to determine μ and μ_f.

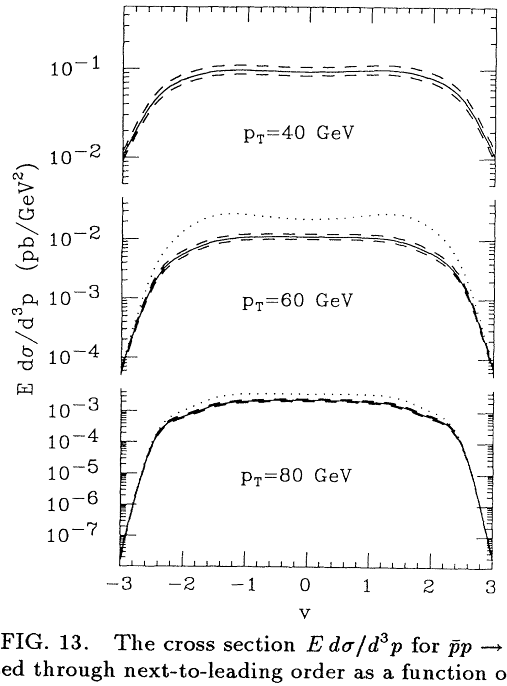

FIG. 13. The cross section $E\,d\sigma/d^3p$ for $\bar{p}p \rightarrow \gamma X$ calculated through next-to-leading order as a function of y and for selected values of p_T at $\sqrt{s} = 1.8$ TeV. The ABFOW parton densities were used. The solid lines show the prediction for the choice $\mu = \mu_f = p_T$. The upper dashed curves correspond to the choice $\mu = \mu_f = \frac{1}{2}p_T$, whereas the lower dashed curves correspond to the choice $\mu = \mu_f = 2p_T$. The dotted lines were obtained after application of the PMS optimization scheme to determine μ and μ_f.

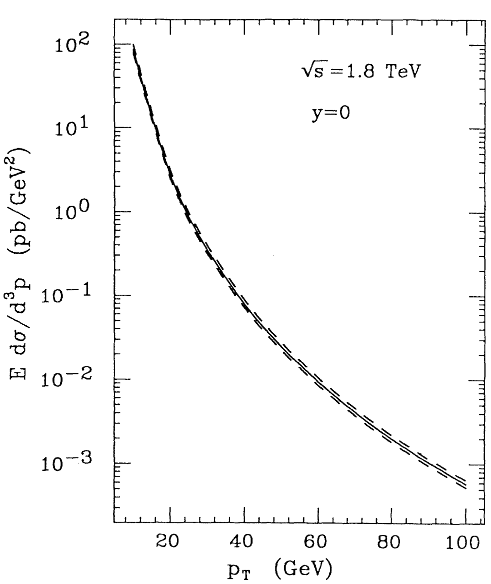

FIG. 14. The cross section $E\,d\sigma/d^3p$ for $\bar{p}p \rightarrow \gamma X$ calculated through next-to-leading order at $y = 0$ as a function of p_T at $\sqrt{s} = 1.8$ TeV. Parton densities with a singular gluon density at small x [Eq. (4.1)] were used. The solid line shows the prediction for the choice $\mu = \mu_f = p_T$. The upper dashed curve corresponds to the choice $\mu = \mu_f = \frac{1}{2}p_T$, whereas the lower dashed curve corresponds to the choice $\mu = \mu_f = 2p_T$.

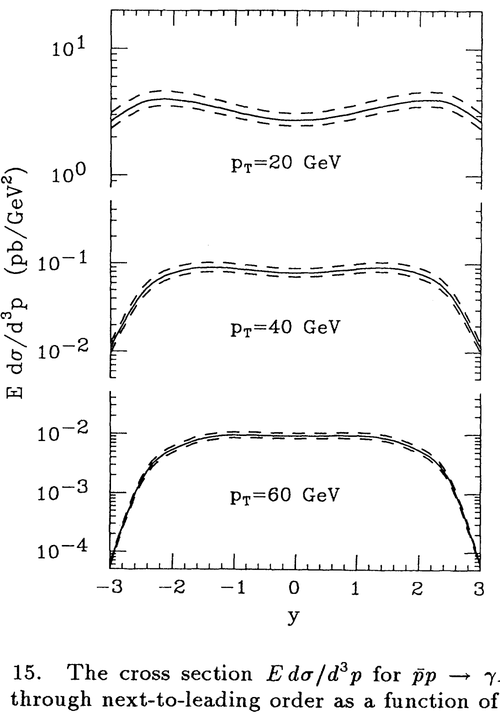

FIG. 15. The cross section $E\,d\sigma/d^3p$ for $\bar{p}p \rightarrow \gamma X$ calculated through next-to-leading order as a function of y and for selected values of p_T at $\sqrt{s} = 1.8$ TeV. Parton densities with a singular gluon density at small x [Eq. (4.1)] were used. The solid lines show the prediction for the choice $\mu = \mu_f = p_T$. The upper dashed curves correspond to the choice $\mu = \mu_f = \frac{1}{2}p_T$, whereas the lower dashed curves correspond to the choice $\mu = \mu_f = 2p_T$.

number near 1 because ϵ is a fixed small number. Since all fragmentation functions, except $D_{\gamma/\gamma}$, should vanish as a power of $(1-z)$, or approach a small fixed number as $z \longrightarrow 1$, the contribution from the fragmentation processes should be limited as ϵ^n with $n \geq 1$. In Fig. 17, we present the ratios of cross sections $E\,d\sigma^{\rm dir}/d^3p$ divided by $E\,d\sigma^{\rm tot}/d^3p$ at the collider energy $\sqrt{s} = 1.8$ TeV for the inclusive and isolated cross sections. Since the isolation cut is not imposed correctly in the program of ABFS, we used the Monte Carlo program developed by Baer *et al.* [7] to calculate this ratio for the isolated cross sections. To obtain the ratios in Fig. 17, we divided the results corresponding to flag $I_{\rm brem} = 1$ by those for $I_{\rm brem} = 3$ in the program of Ref. 7. When $I_{\rm brem} = 1$ the cross section does not include any long-distance fragmentation contribution, while $I_{\rm brem} = 3$ means that the leading-logarithmic fragmentation functions are used. As will be noticed, the calculated ratios in Fig. 17 do not fall along smooth lines. The scatter may be a result of the random numbers generated in the Monte Carlo program, associated with the way the program is written for the case $I_{\rm brem} = 1$. We remark, also, that the solid curve in Fig. 16 and the squares in Fig. 17 represent the same results, in principle, provided the same fragmentation scale is used. However, the fragmentation scale is fixed to be $\sqrt{\hat{s}}$ in the program of ABFS, while it is fixed to be p_T in the program of Baer *et al.* The different choice of the fragmentation scale does not affect the total inclusive cross section much, but it does affect the relative size of the direct and the fragmentation contributions. Because $\sqrt{\hat{s}}$ could be much larger than p_T, the fragmentation contribution in the program of ABFS is larger than that in the program of Baer *et al.* Consequently, the solid curve in Fig. 16 falls below the squares in Fig. 17.

Figure 17 shows that the isolated cross section is insensitive to the contributions from the fragmentation processes. Correspondingly, the isolated photon data should give good constraints on the gluon distributions at collider energies. One may ask how sensitively the cross section depends on the isolation parameters. If the dependence is too great, we must reexamine the value of the data for determining the gluon distribution. Fortunately, as shown in Sec. III both theoretically and numerically, the dependence of the isolated cross sections on the isolation parameters is weak for a wide range of the isolation parameters. Numerical results for the isolated cross sections at different energies can be found in Ref. [7]. One should bear in mind, however, that the second term in Eq.(3.2) was not included in the program developed by Baer *et al.* [7].

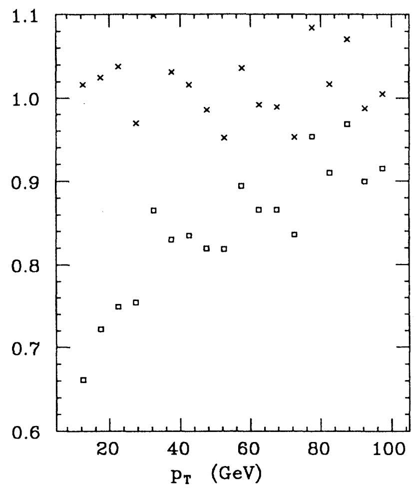

FIG. 17. The ratios of cross sections $E\,d\sigma^{\rm dir}/d^3p$ divided by $E\,d\sigma^{\rm tot}/d^3p$ at $\sqrt{s} = 1.8$ TeV for inclusive photon production (squares), and isolated photon production (crosses), respectively. For the isolated case, $R = 0.7$.

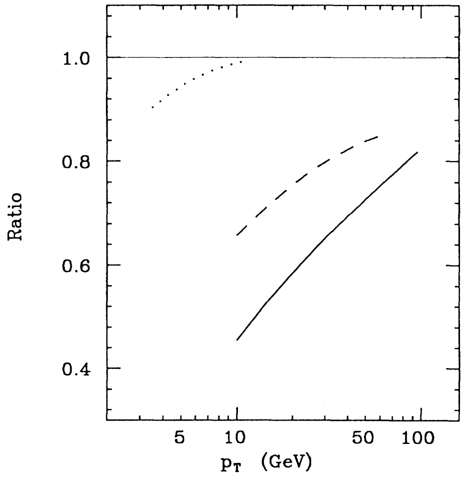

FIG. 16. The ratios of cross sections $Ed\sigma^{\rm dir}/d^3p$ divided by $Ed\sigma^{\rm tot}/d^3p$ at $\sqrt{s} = 30$ GeV (dotted), $\sqrt{s} = 400$ GeV (dashed), and at $\sqrt{s} = 1.8$ TeV (solid), respectively. At $\sqrt{s} =$ 30 GeV and 400 GeV, the results shown are for the case $pp \longrightarrow \gamma X$; at $\sqrt{s} = 1.8$ TeV they are for $\bar{p}p \longrightarrow \gamma X$.

C. Optimization procedure for μ's

The authors of Ref. [5] advocate the PMS scheme, discussed in Sec. II, for determining preferred values of μ and μ_f. In Figs. 12 and 13, we also show predictions at $\sqrt{s} = 1.8$ TeV obtained through application of this procedure. We note that the predicted cross sections are significantly greater (about a factor of 3 at $p_T = 40$ GeV, for example) than those calculated with the choice $\mu = \mu_f = p_T$. We do not show predictions of the PMS scheme for $p_T < 40$ GeV because application of the scheme would require values of μ so small that $(\alpha_s/\pi) > 0.25$. Such values $(\alpha_s > 0.78)$ are unacceptably large.

The very large differences in the predicted rates shown in Figs. 12 and 13 indicate that the choice of scale plays a major role. To illustrate the scale dependence in more detail, we present plots of the cross section versus scale choice in Figs. 18 and 19. In Fig. 18, with the scales μ and μ_f set equal, we see that the cross sections at $p_T = 40$ GeV and $p_T = 80$ GeV decrease monotonically with μ in both the lowest-order and the next-to-leading-order calculations. The variation with μ is substantial at $p_T = 40$ and 80 GeV, and it is even more marked at lower values of p_T. The next-to-leading-order cross sections do not display appreciably less sensitivity to the choice of scale. For $\mu = \mu_f$ there is no solution to the equation $\partial\sigma/\partial\mu = 0$ for values of $\mu > \mu_f^0 = \sqrt{10}$ GeV. (The minimum value of μ_f^0 in the DFLM densities is $\mu_f^0 = \sqrt{10}$ GeV.)

The picture changes somewhat if we relax the condition $\mu = \mu_f$, as shown in Fig. 19. In Fig. 19, the scale μ_f is fixed at $\mu_f = p_T$, and the cross section is plotted versus μ. In this case we observe that a solution does exist at $p_T = 80$ GeV for the equation $\partial\sigma/\partial\mu = 0$, although not at $p_T = 40$ GeV, nor for $p_T < 40$ GeV. The solution at $p_T = 80$ GeV corresponds to a very small value of μ, $\mu < 2$ GeV. We find it difficult to accept the PMS procedure as meaningful since it leads to a scale choice of $\mu \lesssim 2$ GeV when the only physical scale in the problem is as large as $p_T = 80$ GeV.

Since μ is less readily interpreted than values of $\alpha_s(\mu)$, we present in Fig. 20 the calculated cross sections versus values of $\alpha_s(\mu)$. Figures 19 and 20 are two ways to illustrate the same results. For prompt-photon production, the lowest-order results (dot-dashed lines in Fig. 20) necessarily grow linearly with α_s. The next-to-leading-order results are more complicated functions, cf. Eq. (2.2). At $p_T = 40$ GeV, with $\mu_f = p_T$, we see that $\partial\sigma/\partial\alpha_s(\mu) = 0$ has no solution unless $\alpha_s > 1.0$, a value which is uncomfortably large. At $p_T = 80$ GeV, a solution exists with $\alpha_s \simeq 0.25$. We observe that an "optimum" solution appears to exist only for relatively large values of

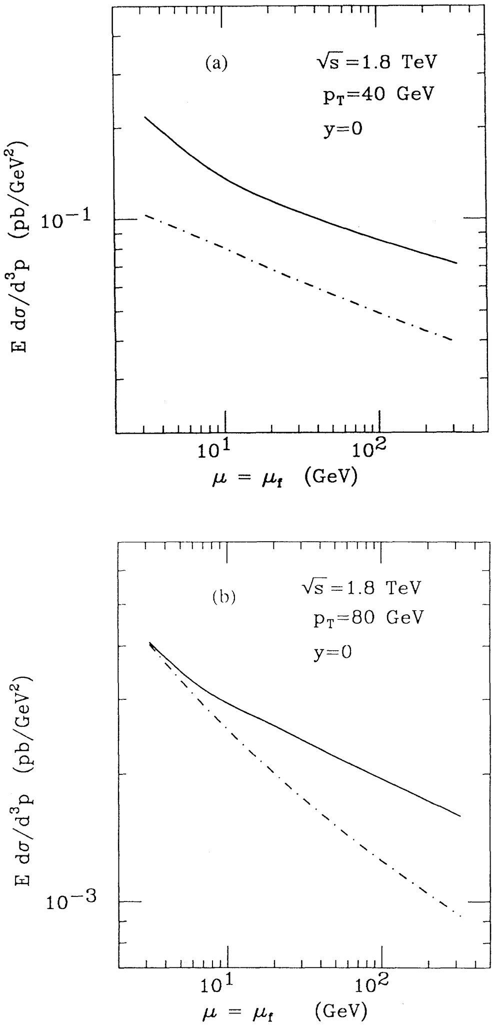

FIG. 18. The cross section $E\,d\sigma/d^3p$ for $\bar{p}p \to \gamma X$ at $\sqrt{s} = 1.8$ TeV, $y = 0$, and (a) $p_T = 40$ GeV, (b) $p_T = 80$ GeV as a function of the scale μ. Calculations are done through next-to-leading order (solid line) and lowest order (dot-dashed line). The DFLM set-2 parton densities were used, with the scales μ and μ_f chosen equal.

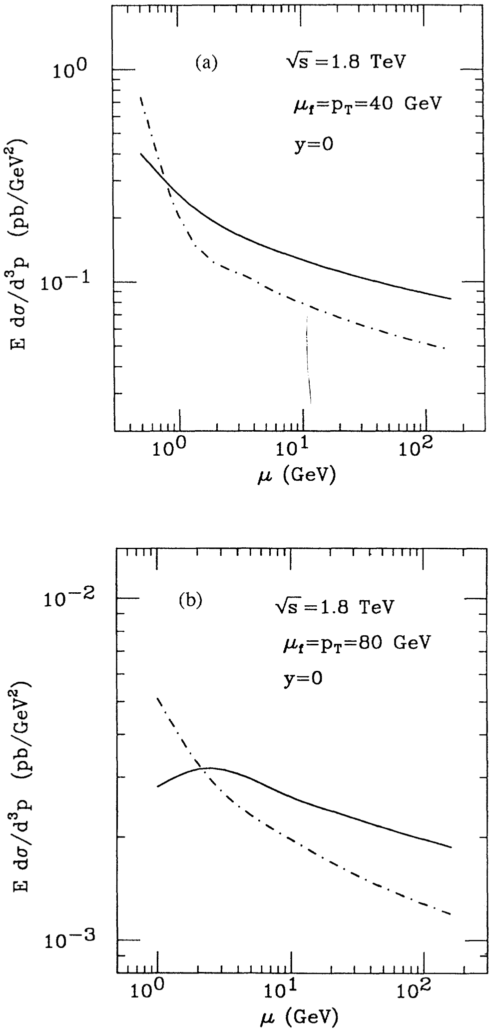

FIG. 19. The cross section $E\,d\sigma/d^3p$ for $\bar{p}p \to \gamma X$ at $\sqrt{s} = 1.8$ TeV, $y = 0$, and (a) $p_T = 40$ GeV, (b) $p_T = 80$ GeV as a function of the scale μ. Calculations are done through next-to-leading order (solid line) and lowest order (dot-dashed line). The DFLM set-2 parton densities were used, with the scale μ_f fixed at $\mu_f = p_T$.

$x_T = 2p_T/\sqrt{s}$. A similar situation is true for hadroproduction of heavy flavors where stability requires that $m_Q/\sqrt{s}$ not be too small [21].

If we allow both μ and μ_f to vary, as advocated by ABFS, the solutions shown by the dotted lines in Figs. 12 and 13 correspond to values of μ and μ_f presented in Table II. Based on these calculations, as well as others done at fixed target energies, we find that the PMS scheme provides values of μ_f which are of order p_T, as would be expected, but values of μ which stay small, $\mu \simeq 1$ GeV. As shown in Table II, an unusual feature is that the values of μ_f do not always grow with p_T. The values of μ also show strong x_F and y dependence.

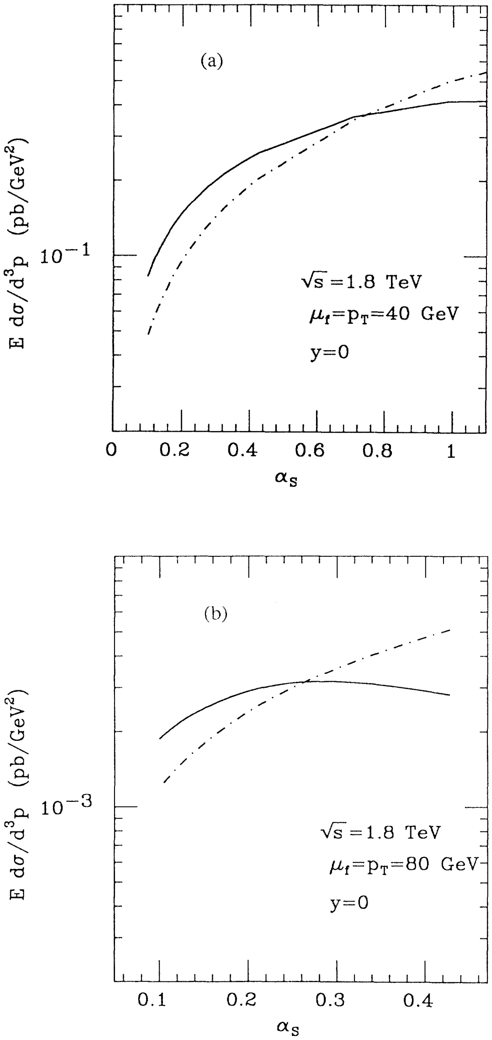

FIG. 20. The cross section $E\,d\sigma/d^3p$ for $\bar{p}p \to \gamma X$ at $\sqrt{s} =$ 1.8 TeV, $y = 0$, and (a) $p_T = 40$ GeV, (b) $p_T = 80$ GeV as a function of $\alpha_s(\mu)$. Calculations are done through next-to-leading order (solid line) and lowest order (dot-dashed line). The DFLM set-2 parton densities were used, with the scale μ_f fixed at $\mu_f = p_T$.

TABLE II. Values of the scales μ and μ_f and of $\alpha_s(\mu)$ obtained from the optimization procedure; $\sqrt{s} = 1.8$ TeV, $y = 0$.

p_T (GeV)	μ_f (GeV)	μ (GeV)	α_s
40	78	0.45	0.72
60	41	0.90	0.39
80	24	2.14	0.26

The values of α_s in Table II, particularly that at $p_T = 80$ GeV, may be compared with determinations of α_s from other processes [22]. Indeed, values are more typically in the range $\alpha_s(\mu) = 0.15 \pm 0.04$ for $\mu > 3$ GeV. The ABFS/PMS scheme seems to produce values of α_s twice as large as anticipated. That being the case, one may be especially uneasy about the size of the uncalculated $O(\alpha_s^3)$ terms in this scheme.

The results reported in this subsection concern the scale dependence of the inclusive cross section. The overall scale dependence is considerably reduced for the isolated photon cross section. As noted earlier, about half of the inclusive cross section is associated with the $O(\alpha_s^2)$ fragmentation contributions. Isolation removes a large part of the fragmentation contribution and thus reduces the importance of $O(\alpha_s^2)$ pieces which are sensitive to the choice of scale.

It is not difficult to understand analytically why μ is forced to be small in the PMS scheme. As in ABFS, we write the cross section, Eq. (2.1), in a form in which the μ and μ_f dependences are manifestly separated:

$$\frac{E d\sigma}{d^3p} = a(\mu)\sigma_{\text{Born}}\left[1 + a(\mu)\tau - a(\mu)\rho(\mu_f, \Lambda)\right]. \tag{4.2}$$

Our Eq. (4.2) is the same as Eq. (2) in Ref. [5]. In Eq. (4.2), $a(\mu) = \alpha_s(\mu)/\pi$, $\tau = b\ln(\mu/\Lambda)$, $b = \beta_0/2$, and σ_{Born} is the convolution of the Born-level hard-scattering cross section with the incident parton densities, $\sigma_{\text{Born}} = \hat{\sigma}_{\text{Born}} \otimes f_1 \otimes f_2$. The function ρ is expressed as

$$\rho = -\left[2\ln\left(\frac{p_T}{\mu_f}\right)\gamma \otimes \hat{\sigma}_{\text{Born}} + H_I\right] \otimes f_1 \otimes f_2/\sigma_{\text{Born}}. \tag{4.3}$$

The finite partonic contribution in next-to-leading-order is represented by H_I plus the $a(\mu)\tau$ term in Eq. (4.2). In Eq. (4.3) γ represents a parton splitting function, and the term proportional to γ is the next-to-leading-order collinear singularity contribution.

We note next that we may expand $\tau = b\ln(\mu/\Lambda)$ obtaining

$$\tau \simeq \frac{1}{a(\mu)} + c\ln\frac{ba(\mu)}{2} + O(a(\mu)), \tag{4.4}$$

where $c = \beta_1/(4\beta_0)$. Taking the derivative $\partial\sigma/\partial a(\mu)$ and setting it to zero, we derive

$$f(a(\mu)) \equiv 2 + a(\mu)\left[c\left(1 + 2\ln\frac{ba(\mu)}{2}\right) - 2\rho\right] = 0. \tag{4.5}$$

It is easy to verify that Eq. (4.5) has *two* solutions, one for $a(\mu) < 1$ and another for $a(\mu) > 1$. By examining the next derivative, $f'(a(\mu))$, one may show that the cross section behaves as a function of $a(\mu)$ as sketched in Fig. 21. The solution with $a(\mu) > 1$ is unphysical since it corresponds to an unacceptable value of $\alpha_s(\mu) > \pi$. We now turn to an examination of the solution with $a(\mu) < 1$.

The solution to Eq. (4.5) with $a(\mu) < 1$ is defined to be the "optimized" $a_{\rm opt}$ ($\equiv \alpha_s(\mu_{\rm opt})/\pi$). By substituting the $a_{\rm opt}$ into Eq. (4.2), we obtain the optimized cross section

$$\frac{Ed\sigma}{d^3p} = a_{\rm opt}\,\sigma_{\rm Born}\left[1 - a_{\rm opt}\left(\frac{c}{2}\right) + O(a_{\rm opt}^2)\right], \tag{4.6}$$

where $c \sim 1.5$. It follows that the ratio of the full cross section in next-to-leading-order to the lowest-order cross section, known as the K factor, is slightly less than unity at $a(\mu) = a_{\rm opt}$. By comparing Eq. (4.2) and Eq. (4.6) at $\mu = \mu_{\rm opt}$, we have

$$b\ln\left(\frac{\mu_{\rm opt}}{\Lambda}\right) - \rho(\mu_f, \Lambda) = -\frac{c}{2}. \tag{4.7}$$

Because of the explicit presence of Λ in the term proportional to $a(\mu)\tau$ in Eq. (4.2), H_I in Eq. (4.3) must contain a term equal to $-b\hat{\sigma}_{\rm Born}\ln(\mu_f/\Lambda)$. Defining $\rho = b\ln(\mu_f/\Lambda) + \rho'$, Eq. (4.7) becomes

$$b\ln\left(\frac{\mu_{\rm opt}}{\mu_f}\right) - \rho'(\mu_f) = -\frac{c}{2}. \tag{4.8}$$

Equation (4.8) shows that to understand why $\mu_{\rm opt}$ is forced to be small is equivalent to knowing the value of $\rho'(\mu_f)$.

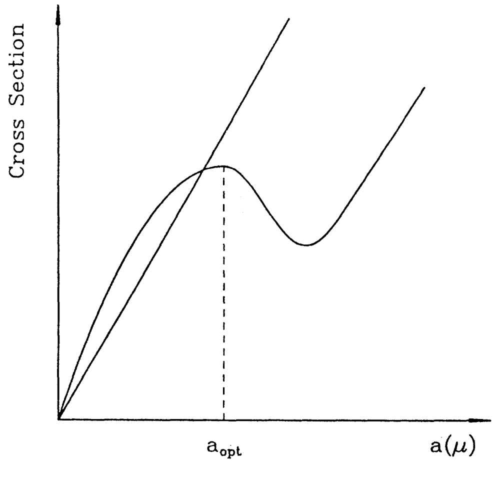

FIG. 21. Sketch of the behavior of the cross section as a function of $a(\mu)$. The dashed line represents the Born-level cross section, and the solid line the cross section including next-to-leading-order contributions.

The exact value of $\rho'(\mu_f)$ certainly depends on μ_f and all kinematic variables (e.g., p_T, y), and it is directly related to the observed K factor, but it does *not* depend explicitly on the value of μ. In terms of $\rho'(\mu_f)$, we rewrite Eq. (4.2) as

$$\frac{Ed\sigma}{d^3p} = a(\mu)\sigma_{\rm Born}\left\{1 + a(\mu)\left[b\ln\left(\frac{\mu}{\mu_f}\right) - \rho'(\mu_f)\right]\right\}, \tag{4.9}$$

and we estimate the value of $\rho'(\mu_f)$ at any given μ_f through the observed K factor. By choosing $\mu = \mu_f$ in Eq. (4.9), we see that the K factor at $\mu = \mu_f$ is given by $1 - a(\mu_f)\rho'(\mu_f)$, and then

$$-\rho'(\mu_f) = \frac{K-1}{a(\mu_f)} \approx (K-1)\,b\ln\left(\frac{\mu_f}{\Lambda}\right). \tag{4.10}$$

Substituting $-\rho'(\mu_f)$ from Eq. (4.10) into Eq. (4.8), we obtain

$$\mu_{\rm opt} \approx \Lambda\left(\frac{\Lambda}{\mu_f}\right)^{K-2} e^{-c/2b}. \tag{4.11}$$

It is known that at $\mu = \mu_f \sim p_T$, the K factor is much larger than 1 and closer to 2 for most values of kinematic variables. Therefore, the right-hand side of Eq. (4.11) is very small and is of order of Λ. As a result, $\mu_{\rm opt}$ is forced to be of order of Λ; $a_{\rm opt}$ is always large and not very sensitive to the specific values of the kinematic variables.

We conclude from Eq. (4.8) that $\rho'(\mu_f)$ has to be extremely small in order to have $\mu_{\rm opt}$ of order μ_f which is of order of p_T. This case can happen only when $x_T = 2p_T/\sqrt{s}$ is very large. For the interesting kinematic region where x_T is small, the optimization scheme may result in a very large value of α_s. When α_s is so large, we would feel uncomfortable without checking the size of the next-order corrections at the same α_s.

V. SUMMARY AND PROSPECTS

Several issues were examined in this paper, all concerned with the applicability and reliability of perturbative QCD calculations of prompt-photon production at collider energies. We began by distinguishing calculations of the inclusive prompt-photon cross section from those of the isolated prompt-photon cross section. It is the isolated cross section that is most readily determined experimentally at collider energies. In principle, the inclusive cross section is better defined theoretically. However, as discussed in our earlier paper [3] and developed in more detail here, the constraint of photon isolation can be incorporated consistently in the short-distance perturbative calculation, and theoretically reliable expressions can be derived for isolated photon cross sections.

Important sources of practical uncertainty are present for both the inclusive and the isolated cases since cross sections depend to a greater or lesser extent on the following unknowns: the nonperturbative long-distance photon fragmentation functions, the gluon parton densities, and the renormalization, factorization, and fragmentation scales (μ, μ_f, and μ_F). The data provide correlated information on the three unknowns. If the oft-stated goal is the determination of the gluon density, then it is necessary first to somehow constrain the other two unknowns.

An important advantage of photon isolation is that isolation significantly reduces the contribution from photon fragmentation processes. (These are a generalization of what have been often termed "bremsstrahlung" contributions.) Moreover, what remains of the fragmentation contribution is the contribution of $D(z)$ at large z, $z > 1/1+\epsilon$, where theoretical constraints are most reliable. Thus, there is reason to think that isolated photon data at collider energies, with their significantly reduced sensitivity to fragmentation effects, will eventually satisfy their promise of determining the gluon density. Further detailed investigation of fragmentation models must be undertaken before a firm conclusion can be delivered.

The remaining uncertainty, that of scale dependence, is more problematic. As we showed by explicit calculation, the variation of the next-to-leading-order cross section when $\mu = \mu_f$ is varied over the limited range of 0.5 $p_T < \mu < 2p_T$ is as great as the variation associated with changes in the gluon density. In Sec. IV C we examined schemes proposed for fixing the choice of scale. Optimized scales can lead to significant increases in cross section but at the expense of reductions in μ or μ_f to values we would consider unacceptably small. Such small values point theoretically to the need to examine and possibly resume a series in $\alpha_s \ln(p_T/\mu)$.

The issue of the increased sensitivity of cross sections to μ for relatively small values of $p_T/\sqrt{s}$ is not unique to prompt-photon production. A similar situation occurs for heavy flavor production when the ratio of the quark mass m_q to $\sqrt{s}$ becomes small; e.g., bottom quark production at collider energies [23]. As the ratio $p_T/\sqrt{s}$ in prompt-photon production decreases, or as $m_q/\sqrt{s}$ for heavy flavor production decreases, higher-order processes controlled by t-channel gluon exchange grow in importance relative to the lowest-order fermion-exchange diagrams (Fig. 1). The different asymptotic behaviors result in increased sensitivity to μ at small $p_T/\sqrt{s}$. Collider data at $\sqrt{s} = 1.8$ TeV and $p_T \leq 50$ GeV appear to fall in this domain.

As will be noted, there are systematic discrepancies between the theoretical curves and the data in Fig. 10. The data appear to fall more steeply as a function of p_T, and theory tends to fall below the data in magnitude in the small p_T region. Since the data include an isolation cut whereas the theory curves in Fig. 10 do not, the discrepancies would be greater if an isolation cut were made on the theory. We believe the discrepancies are indicative of two effects. First, and the more important, in the small p_T region at collider energies, $x_T = 2p_T/\sqrt{s}$ is small. This is the "semihard" region where $\ln x_T$ can be large and higher-order contributions can be very important. In recent work on heavy flavor production, Collins and Ellis [24] have addressed an analogous case for small $x = m_q/\sqrt{s}$. They show that large logarithms associated with t-channel gluon exchange can be resummed, and they obtain substantial increases in the cross section at small x. We believe a similar situation will be true at small x_T for prompt-photon production since t-channel gluon diagrams are present in higher order in this case also.

A better understanding of the fragmentation contribution should also lead to improved agreement with data. Photons from the hard-scattering diagrams tend to have a relatively shallow p_T distribution whereas those from fragmentation fall more steeply in p_T owing to the behavior of $D(z)$ and the $1/z^2$ factor in Eq. (2.1). There is no absolute separation between these two contributions since different choices of μ_F correspond to different partitions. A decrease of μ_F would increase the relative size of the short-distance contribution at small p_T.

The importance of fragmentation contributions argues for substantial theoretical work to improve our present level of understanding and to constrain models of fragmentation functions. Explicit expressions must be derived to account for the resummation of t-channel gluon-exchange effects at small x_T. In future work, efficient numerical programs must also be devised to include isolation restrictions in a fully accurate and consistent fashion.

ACKNOWLEDGMENTS

We have benefited from discussions with G. Sterman, G.T. Bodwin, R.K. Ellis, R.M. Harris, J.F. Owens, and W.K. Tung. The research was supported in part by the U.S. Department of Energy, Division of High Energy Physics, Contract No. W-31-109-ENG-38; and by National Science Foundation Grant No. PHY-89-08495.

---

[1] E. L. Berger, E. Braaten, and R. D. Field, Nucl. Phys. **B239**, 52 (1984), and references therein; J. F. Owens, Rev. Mod. Phys. **59**, 465 (1987); for a recent survey of data, consult J. Huston, in *Proceedings of the XIVth International Symposium on Lepton and Photon Interactions*, Stanford, California, 1989, edited by M. Riordan (World Scientific, Singapore, 1990), p. 348.

[2] E. L. Berger and J. Qiu, Phys. Lett. B **248**, 371 (1990); an earlier version of the current paper appeared and was circulated as Argonne Report No. ANL-HEP-PR-89-108, 1989 (unpublished).

[3] UA2 Collaboration, R. Ansari *et al.*, Phys. Lett. B **176**, 239 (1986); Z. Phys. C **41**, 395 (1988); UA1 Collaboration, C. Albajar *et al.*, Phys. Lett. B **209**, 385 (1988); **209**, 397 (1988); CDF Collaboration, R. M. Harris *et al.*, in *Proceedings of the Workshop on Hadron Structure Functions and Parton Distributions*, Fermilab, 1990, edited by D.F. Geesaman *et al.* (World Scientific, Singa-

pore, 1990), p. 278.

[4] R. K. Ellis, comment at the Workshop on Hadron Structure Functions and Parton Distributions, Fermilab, 1990 (unpublished).

[5] P. Aurenche, R. Baier, M. Fontannaz, and D. Schiff, Nucl. Phys. **B297**, 661 (1988).

[6] A. P. Contogouris, S. Papadopoulos, and D. Atwood, McGill University report, 1989 (unpublished).

[7] H. Baer, J. Ohnemus, and J. F. Owens, Phys. Rev. D **42**, 61 (1990).

[8] P. Aurenche, R. Baier, M. Fontannaz, J. F. Owens, and M. Werlen, Phys. Rev. D **39**, 3275 (1989).

[9] E. L. Berger, Z. Phys. C **4**, 289 (1980); E. L. Berger, Phys. Rev. D **26**, 105 (1982); J. W. Qiu, *ibid.* **42**, 30 (1990); J. W. Qiu and G. Sterman, Nucl. Phys. **B353**, 105 (1991); **B353**, 137 (1991).

[10] J. C. Collins and W. K. Tung, Nucl. Phys. **B278**, 934 (1986).

[11] M. Diemoz, F. Ferroni, E. Longo, and G. Martinelli, Z. Phys. C **39**, 21 (1988).

[12] A. D. Martin, R. G. Roberts, and W. J. Stirling, Phys. Rev. D **37**, 1161 (1988); P. N. Harriman, A. D. Martin, R. G. Roberts, and W. J. Stirling, *ibid.* **42**, 798 (1990); J. Kwiecinski, A. D. Martin, W. J. Stirling, and R. G. Roberts, *ibid.* **42**, 3645 (1990).

[13] J. G. Morfin and W.K. Tung, Fermilab Report No. FNAL-PUB-90/74, 1990 (unpublished).

[14] Owens (Ref. [1]); J.F. Owens and J. Qiu, in *Research Directions for the Decade*, Proceedings of the Summer Study, Snowmass, Colorado, 1990 (Editions Frontieres, Gif-sur-Yvette, France, in press).

[15] Owens (Ref. [1]).

[16] G. Grunberg, Phys. Rev. D **29**, 2315 (1984).

[17] P. M. Stevenson, Phys. Rev. D **23**, 2916 (1981); Nucl. Phys. **B203**, 472 (1982); H. D. Politzer, *ibid.* **B194**, 493 (1982); P. M. Stevenson and H. D. Politzer, *ibid.* **B277**, 758 (1986).

[18] CDF Collaboration, Harris *et al.* (Ref. [3]).

[19] F. E. Low, Phys. Rev. **111**, 974 (1958); G. McKeon, Phys. Rev. D **15**, 3668 (1977).

[20] A. H. Mueller, Phys. Rev. D **20**, 2037 (1979); J. C. Collins and D. E. Soper, Nucl. Phys. **B193**, 381 (1981); A. Sen, Phys. Rev. D **24**, 3281 (1981); J. G. M. Gatheral, Phys. Lett. **133B**, 90 (1983).

[21] G. Altarelli, M. Diemoz, G. Martinelli, and P. Nason, Nucl. Phys. **B308**, 724 (1988).

[22] For a compilation, see R. K. Ellis, in *Proceedings of the XXIV International Conference on High Energy Physics*, Munich, 1988, edited by R. Kotthaus and J. H. Kuhn (Springer-Verlag, Berlin, 1989), p. 48.

[23] R. K. Ellis and G. A. Ross, Nucl. Phys. **B345**, 79 (1990); R. K. Ellis, *Proceedings of the Workshop on Hadron Structure Functions and Parton Distributions* (Ref. [3]), p. 405.

[24] J. C. Collins and R. K. Ellis, Fermilab Report No. FERMILAB-Pub-91/22T (unpublished).